

**Best Available  
Copy  
for all Pictures**

AD-A007 791

LASER WINDOW SURFACE FINISHING AND COATING TECHNOLOGY

HUGHES RESEARCH LABORATORIES

PREPARED FOR

AIR FORCE CAMBRIDGE RESEARCH LABORATORIES

DEFENSE ADVANCED RESEARCH PROJECTS AGENCY

JANUARY 1975

DISTRIBUTED BY:

**NTIS**

National Technical Information Service  
U. S. DEPARTMENT OF COMMERCE

State Section	<input type="checkbox"/>
Ad. Section	<input type="checkbox"/>
	<input type="checkbox"/>
ABILITY CODE	
and/or SPECIAL	

MS

Qualified requestors may obtain additional copies from  
Defense Documentation Center. All others should  
contact the National Technical Information Service.

UNCLASSIFIED

SECURITY CLASSIFICATION OF THIS PAGE (When Data Entered)

REPORT DOCUMENTATION PAGE		READ INSTRUCTIONS BEFORE COMPLETING FORM
1. REPORT NUMBER AFCRL-TR-75-0041	2. GOVT ACCESSION NO.	3. RECIPIENT'S CATALOG NUMBER
4. TITLE (and Subtitle) LASER WINDOW SURFACE FINISHING AND COATING TECHNOLOGY		5. TYPE OF REPORT & PERIOD COVERED Final Report 1 May 1973 to 31 January 1975
		6. PERFORMING ORG. REPORT NUMBER
7. AUTHOR(s) S. D. Allen, A.I. Braunstein, M. Braunstein, A. L. Gentile, C.R. Giuliano, R.R. Hart, R.R. Turk, V. Wang, D. Zuccaro		8. CONTRACT OR GRANT NUMBER(s) F19628-73-C-0243
9. PERFORMING ORGANIZATION NAME AND ADDRESS Hughes Research Laboratories 3011 Malibu Canyon Road Malibu, CA 90265		10. PROGRAM ELEMENT PROJECT, TASK AREA & WORK UNIT NUMBERS 6110E, 2415, T and WU, n/a BPAC n/a
11. CONTROLLING OFFICE NAME AND ADDRESS Air Force Cambridge Research Labs Hanscom AFB, Mass. 01731 Contract Monitor: Dr. Harold Posen/LOO		12. REPORT DATE January 1975
		13. NUMBER OF PAGES 103
14. MONITORING AGENCY NAME & ADDRESS (if different from Controlling Office)		15. SECURITY CLASS (of this report) Unclassified
		15a. DECLASSIFICATION DOWNGRADING SCHEDULE
16. DISTRIBUTION STATEMENT (of this Report) Approved for public release; distribution unlimited.		
17. DISTRIBUTION STATEMENT (of the abstract entered in Block 20, if different from Report)		
18. SUPPLEMENTARY NOTES Sponsored by Defense Advanced Research Projects Agency. ARPA Order No. 2415.		
19. KEY WORDS (Continue on reverse side if necessary and identify by block number) Laser Windows, Surface Finishing, Thin Films, Antireflection Coatings, 10.6 $\mu$ m, 5 $\mu$ m, Laser Damage Studies, Surface Characterization, Optical Evaluation, Potassium Chloride, Zinc Selenide, Alloys of Halides, Calcium Fluoride		
20. ABSTRACT (Continue on reverse side if necessary and identify by block number) We report on the objectives and the progress achieved in a program to study the surface finishing and coating of laser windows. The program covered six areas of study: surface finishing, surface characterization, coating techniques, optical evaluation, chemical analysis, and laser window damage studies. Potassium chloride surfaces have been produced on reactive atmosphere processed (RAP) KCl using HCl		

DD FORM 1 JAN 73 1473

EDITION OF 1 NOV 65 IS OBSOLETE

UNCLASSIFIED

SECURITY CLASSIFICATION OF THIS PAGE (When Data Entered)

PRICES SUBJECT TO CHANGE

Reproduced by  
NATIONAL TECHNICAL  
INFORMATION SERVICE  
US Department of Commerce  
Springfield, VA. 22151



UNCLASSIFIED

SECURITY CLASSIFICATION OF THIS PAGE (When Data Entered)

etching which show an order of magnitude improvement in KCl surface damage resistance.

Surface damage level approaches the bulk level in some KCl samples. KCl surface damage levels  $>1500 \text{ J/cm}^2$  for 600 nsec pulses have been obtained with bulk damage levels  $>3000 \text{ J/cm}^2$  at the same pulse duration. An etch-polish procedure is reported for ZnSe which results in a significant decrease in surface absorption. An inverse dependence of  $10.6 \mu\text{m}$  optical absorption on film deposition rate is reported for germanium films,  $\beta$  of  $\approx 10 \text{ cm}^{-1}$  is reported for the best films. The important parameters controlling the absorption of these films are found to be the presence of heavy metal impurities and possibly physical structure. Ultrahigh vacuum deposited  $\text{ThF}_4$  films were found to have minimum absorptions of  $\approx 10 \text{ cm}^{-1}$ . The controlling parameter in this case is substrate temperature. Ion beam sputtering of  $\text{ThF}_4$  using pure argon ion beams results in films deficient in fluorine having high optical absorption at  $10.6 \mu\text{m}$ . Reactive sputtering in argon-fluorine gas mixtures may be required for producing stoichiometric fluoride films. Rutherford backscattering for chemical analysis of films and window surface structure promises to be a new powerful technique for such studies, using moderate beam energies of  $180 \text{ KeV H}^+$  and  $280 \text{ KeV H}^{++}$ . A unique modulated light ellipsometer which can operate over a broad wavelength range in the uv, visible, near IR, and  $10.6 \mu\text{m}$  was constructed.

UNCLASSIFIED

SECURITY CLASSIFICATION OF THIS PAGE (When Data Entered)

## TABLE OF CONTENTS

SECTION		PAGE
	LIST OF ILLUSTRATIONS . . . . .	5
I	INTRODUCTION . . . . .	9
II	TECHNICAL DISCUSSION . . . . .	11
	A. Surface Finishing . . . . .	11
	B. Surface and Chemical Characterization . . . . .	26
	C. Coating Techniques . . . . .	41
	D. Optical Evaluation . . . . .	60
	E. 10.6 $\mu\text{m}$ Laser Damage . . . . .	62
III	SUMMARY . . . . .	97
	REFERENCES . . . . .	99
	APPENDIX . . . . .	103

# LIST OF ILLUSTRATIONS

FIGURE		PAGE
1	Optical micrographs of KCl under bright field illumination (500x) . . . . .	13
2	Optical micrographs of KCl under oblique lighting conditions (500x) . . . . .	14
3	Optical micrographs of KCl under phase contrast illumination (500x) . . . . .	15
4	Optical micrographs of KCl under phase contrast illumination (325x) . . . . .	16
5	SEM surface topography of KCl surface mechanically polished and etched in HCl (15,000x) . . . . .	17
6	SEM photographs of KCl surface at a beam voltage of 20 kV . . . . .	18
7	Optical micrographs of press-forged KCl after 1 min HCl etch . . . . .	20
8	Photomicrographs of ZnSe surfaces after removal of polished surface layer (325x). . . . .	22
9	Photomicrographs of ZnSe surfaces after mechanical polishing and after final etch polishing (325x) . . . . .	25
10	Schematic of ion backscattering target chamber . . . . .	28
11	140 keV $H^+$ channeling analysis of polished KCl before and after 300°C anneal . . . . .	28
12	140 keV $H^+$ channeling analysis of polished and etched KCl . . . . .	30
13	Backscattered energy spectra of 140 keV protons . . . . .	31
14	Backscattered energy spectrum of 280 keV $He^{++}$ . . . . .	33

FIGURE		PAGE
15	Backscattered energy spectrum of 280 keV He <sup>++</sup> incident on a 125 Å UHV deposited Ge film on KCl . . . . .	34
16	Backscattered energy spectrum of 280 keV H <sup>++</sup> incident on a 150 Å Ge film sputter deposited onto a carbon substrate . . . . .	36
17	Auger electron analysis of a 175 Å UHV deposited Ge film on KCl . . . . .	37
18	Electron microprobe analysis of a 1.25 μm UHV deposited Ge film on KCl . . . . .	38
19	Backscattered energy spectrum of 280 keV He <sup>++</sup> incident on a thin germanium film evaporated onto KCl in UHV . . . . .	40
20	Backscattered energy spectrum of 280 keV He <sup>++</sup> incident on a 1350 Å germanium film evaporated onto KCl . . . . .	42
21	10.6 μm absorption versus deposition rate for UHV germanium . . . . .	45
22	Backscattered energy spectrum of 280 keV He <sup>++</sup> incident on ThF <sub>4</sub> film evaporated onto a carbon substrate . . . . .	49
23	PVD apparatus . . . . .	52
24	CVD apparatus . . . . .	54
25	Chemical vapor deposition of As <sub>2</sub> S <sub>3</sub> . . . . .	55
26	Dimorphite crystals on As <sub>2</sub> S <sub>3</sub> matrix — KCl substrate . . . . .	57
27	Crystal "islands" on As <sub>2</sub> S <sub>3</sub> matrix . . . . .	58
28	As <sub>2</sub> S <sub>3</sub> deposition on uncoated and precoated KCl substrate . . . . .	58
29	(a) Deposition at low temperature on previously coated KCl. (b) Deposition at lower temperature on uncoated KCl . . . . .	59



FIGURE		PAGE
30	Schematic of TEA laser cross section . . . . .	63
31	Simplified schematic of double discharge electrical pulse forming network. Ignitron . . . . .	65
32	Simplified schematic of double discharge electrical pulse forming network. Thyatron . . . . .	65
33	Gas handling system . . . . .	66
34	(a) Schematic of optical train. (b) Damage facility . . . . .	67
35	Second model of sample chamber . . . . .	71
36	(a) Pulse shape measured with photon drag detector. (b) 0.6 $\mu$ sec equivalent pulse length . . . . .	75
37	Definition of equivalent pulse . . . . .	78
38	(a) Etch polished HRL RAP KCl. (b) Con- ventionally polished HRL RAP KCl . . . . .	87
39	Surface damage on conventionally polished KCl . . . . .	88
40	Surface damage on etch-polished KCl. . . . .	88
41	ZnSe window damaged by a 10.6 $\mu$ m pulsed laser beam . . . . .	94

## FOREWORD

This program was sponsored by the Defense Advanced Research Projects Agency, monitored by Air Force Cambridge Research Laboratories, Air Force Systems Command, United States Air Force, Bedford, Massachusetts, under Contract F19628-73-C-0243. The program was directed by M. Braunstein. The principal investigator was M. Braunstein. Contributors to the program included S. D. Allen, A. I. Braunstein, A. L. Gentile, C. R. Giuliano, R. R. Hart, R. R. Turk, V. Wang, and D. Zuccaro.

## I. INTRODUCTION

Hughes Research Laboratories (HRL) has conducted a broad program to develop laser window surface finishing and coating technology. Extensive investigations are under way in many laboratories throughout the country, as well as at HRL to develop window materials that have both the low-optical absorption and the high tensile yield stress necessary to satisfy system applications. Two classes of materials — the wide bandgap semiconductors and the alkali halides — have received major emphasis in these investigations. The goal of our program at HRL was to investigate the surface characteristics and the optical coatings applied to laser windows in order to develop optimized finishing and coating procedures so that the laser damage thresholds of the coatings and surfaces approximate as closely as possible the damage thresholds of the bulk window materials. At present, serious limitation to window performance characteristics can exist because as the laser pulse duration is shortened and the peak power densities rise, the low damage threshold of some of the presently available coatings and surfaces can cause damage to occur below the bulk material damage threshold. This lowered damage threshold, caused by the presence of pores and microcracks which can be present in window surfaces and coatings, was the subject of a report by Bloembergen and Stickley<sup>1</sup> which focused early attention on the importance of launching a research effort on surfaces and coatings to provide improvements in the state of the art.

The program which we have conducted in the period from 1 May 1973 to 31 October 1974 consisted of a broad attack on some of the major problem areas in the surface finishing and coating of windows for use at the 10.6  $\mu\text{m}$   $\text{CO}_2$  laser wavelength. Early emphasis was placed on the ability to prepare reproducible surfaces on KCl and ZnSe which were free of impurities and were structurally representative of the bulk materials.

Success in this effort guaranteed that a "standard surface" was available for use in the subsequent coating work which had as its goal the exploration of the potential of film preparation technologies other than sublimation or evaporation in conventional vacuum systems. These included deposition in ultrahigh vacuum, sputtering, physical vapor deposition, and chemical vapor deposition. Laser damage studies were conducted with the goal of determining the damage thresholds and elucidating the damage mechanisms of the window materials, both in the bulk and on the surface, and the coatings applied to them.

An important aspect of the program was the extensive chemical, physical, and optical characterization of surfaces and films. The effort had a twofold goal: first, to track progress and aid in the conduct of the work on the other tasks, and second, to assess the potential of the various instruments and techniques. The various surface physics tools used included electron microprobe analysis, Rutherford backscattering of light ions, Auger electron spectroscopy, low energy electron diffraction, and scanning electron microscopy.

CO<sub>2</sub> laser calorimetry to determine the 10.6  $\mu\text{m}$  absorption of films and surfaces was used extensively. Other standard optical evaluation methods used were infrared spectrophotometry, attenuated total reflection spectroscopy, and 10.6  $\mu\text{m}$  scattering and reflectance.

In addition, a unique optical evaluation tool was developed in the form of a modulated light ellipsometer for use at 10.6  $\mu\text{m}$ . This instrument can be used for the precise determination of the optical constants of surfaces and films and is expected to be competitive with calorimetry for the determination of absorption coefficients for interfaces and films.

As a result of the work performed on this program five papers were presented: one at the Third Conference on High Power Infrared Laser Window Materials (1973), two at the 1974 Symposium on Damage in Laser Materials, and two at the Fourth Conference on High Power Infrared Laser Window Materials (1974).



## II. TECHNICAL DISCUSSION

### A. Surface Finishing

Conventional optical surface finishing techniques used in the optical industry use mechanical grinding, lapping, and polishing procedures which make it very difficult to attain surfaces of high grade optical finish on materials that are as soft as those under investigation for use as infrared windows. In our work, we have studied ion beam polishing procedures and mechanical-chemical, etch-polish techniques for obtaining optical surfaces that are free of surface scratches and digs and that have surface work damage minimized. The mechanical-chemical polishing procedures for KCl and ZnSe have resulted in lower 10.6  $\mu\text{m}$  absorption in the finished optical blanks, and surfaces which have much improved laser damage resistance.

#### 1. KCl Finishing

The mechanical-chemical polishing techniques for KCl are an extension of the KCl finishing procedures reported by Braunstein, et al.<sup>2</sup> The technique reported in that work has been complemented with a final chemical etching procedure using concentrated HCl based on a modification of the work reported by Davisson<sup>3</sup> of the U. S. Naval Research Laboratory.

In our experiments, 25 mm by 9 mm thick blanks of HRL reactive atmosphere process (RAP) grown KCl were sliced from a crystal boule with a wire saw and mechanically polished to a "window" finish and potted in Carbolene plastic film. The samples were subjected to a series of three-minute etches in reagent grade concentrated HCl after removal of the Carbolene layer followed by a rinsing with 100% ethanol (glass wash bottle) and drying in a dry nitrogen stream. The initial samples were not agitated during the etching and after the third etch (total nine minutes) most of the initial polishing scratches as observed under 500x optical magnification (Bausch and Lomb Research Metallograph) were removed. The surface was

generally smooth between the remaining scratches and grain boundaries, although some small roughly circular marks were observable which looked like rinsing marks. After a fourth three-minute etch definite etch pits were evident on the surface under the same magnification. Surfaces etched in HCl even for a short period of time do not show evidence of the surface fogging that occurs on polished surfaces produced using only mechanical finishing.

An optically polished window blank of the size referred to above, flat to approximately two fringes at  $6328 \text{ \AA}$  was characterized immediately after polishing by absorption calorimetry, dark, bright, and oblique field optical microscopy and phase contrast microscopy. The latter technique tends to show subsurface damage that normally cannot be seen with the other optical microscope techniques. The same tests were repeated after two thirty-second etches in concentrated HCl with agitation followed by ethanol rinsing and drying as discussed above. The results are shown in Figs. 1 through 4(a), (b), and (c), respectively. Figure 5 shows a scanning electron microscope photograph (SEM) taken at  $\sim 15,000\times$ . In Fig. 6(a), (b), and (c) are shown additional SEM photographs of a typical etched KCl surface at  $9,000\times$ ,  $18,000\times$ , and  $18,000\times$ , respectively, at a beam voltage of 20 kV and  $\approx 70^\circ$  tilt to the sample surface. Views a and b are of a surface region near grain boundaries and c is of a more typical surface region. The photograph in Fig. 1(c) shows no scratches or blemishes observable at  $500\times$  magnification other than grain boundaries. Twyman-Green interferometer photographs indicate that the flatness deteriorated by about a factor of two as a result of the total one-minute etch. The  $10.6 \mu\text{m}$  absorption was reduced for KCl surfaces etched in HCl using the above procedures. Hughes Research Laboratories RAP grown KCl crystals after mechanical polishing have absorptions in the range of  $0.0003 \text{ cm}^{-1}$  to  $0.0005 \text{ cm}^{-1}$ , after chemical etching absorptions are in the  $0.00015 \text{ cm}^{-1}$  to  $0.00020 \text{ cm}^{-1}$  range.

An attenuated total internal reflection plate (ATR)  $5 \text{ cm} \times 2 \text{ cm} \times 2 \text{ cm}$  with  $45^\circ$  angles at entrance faces was fabricated from RAP KCl

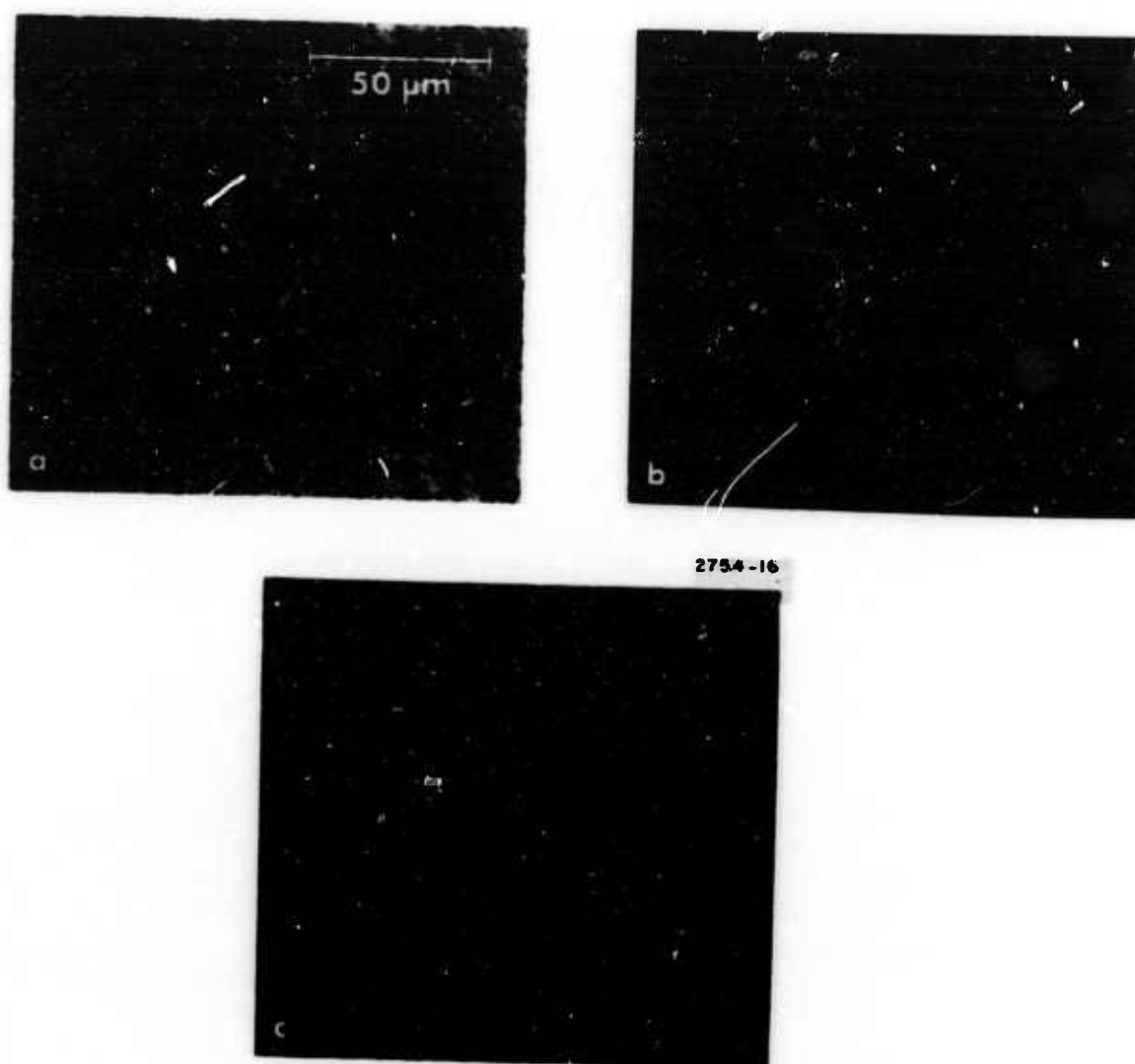


Fig. 1. Optical micrographs of KCl under bright field illumination (500 x).

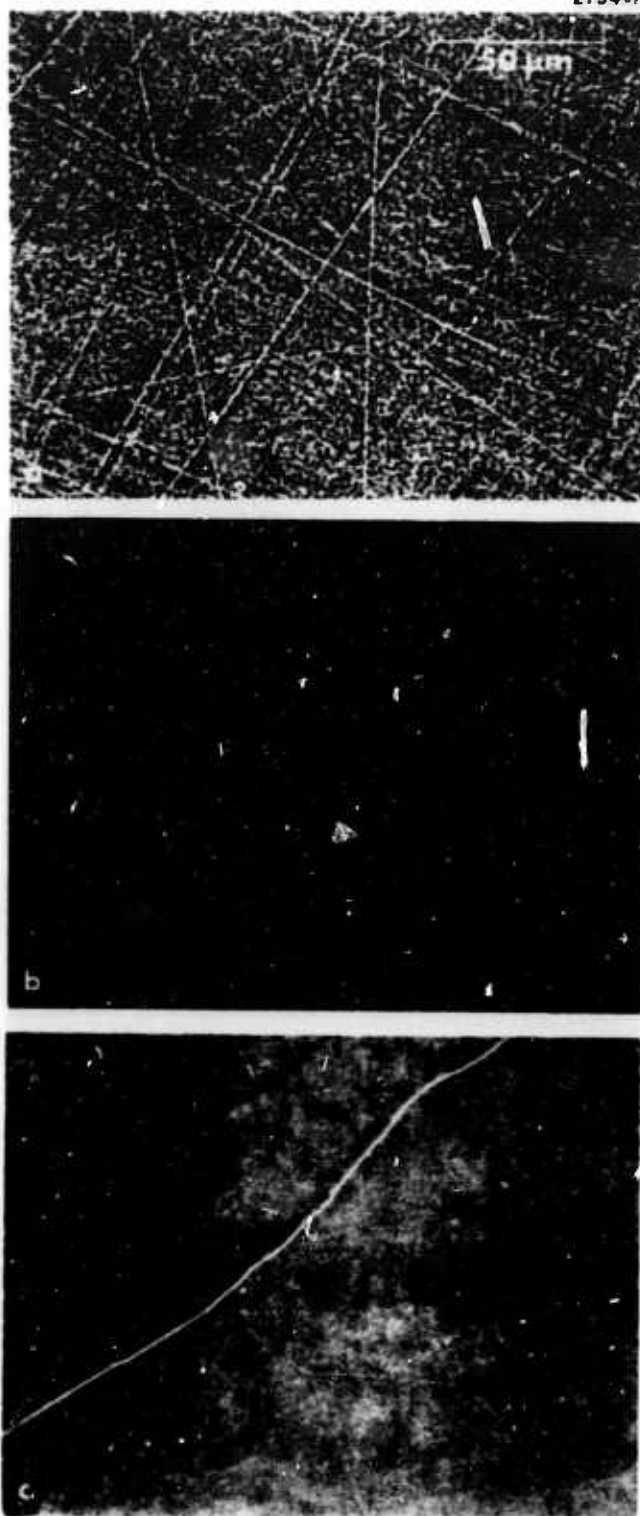


Fig. 2.  
Optical micrographs of KCl under oblique  
lighting conditions (500 $\times$ ).



2754-11



Fig. 3.  
Optical micrographs of KCl under phase  
contrast illumination (500x).



Fig. 4.  
Optical micrographs of KCl under phase  
contrast illumination (325x).

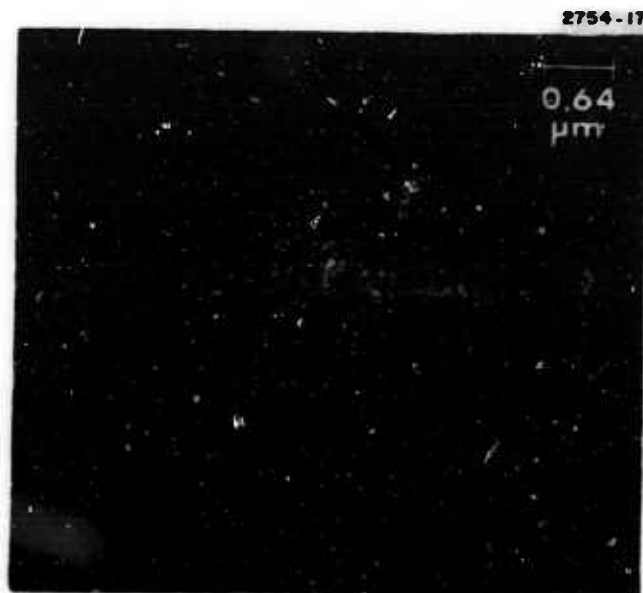
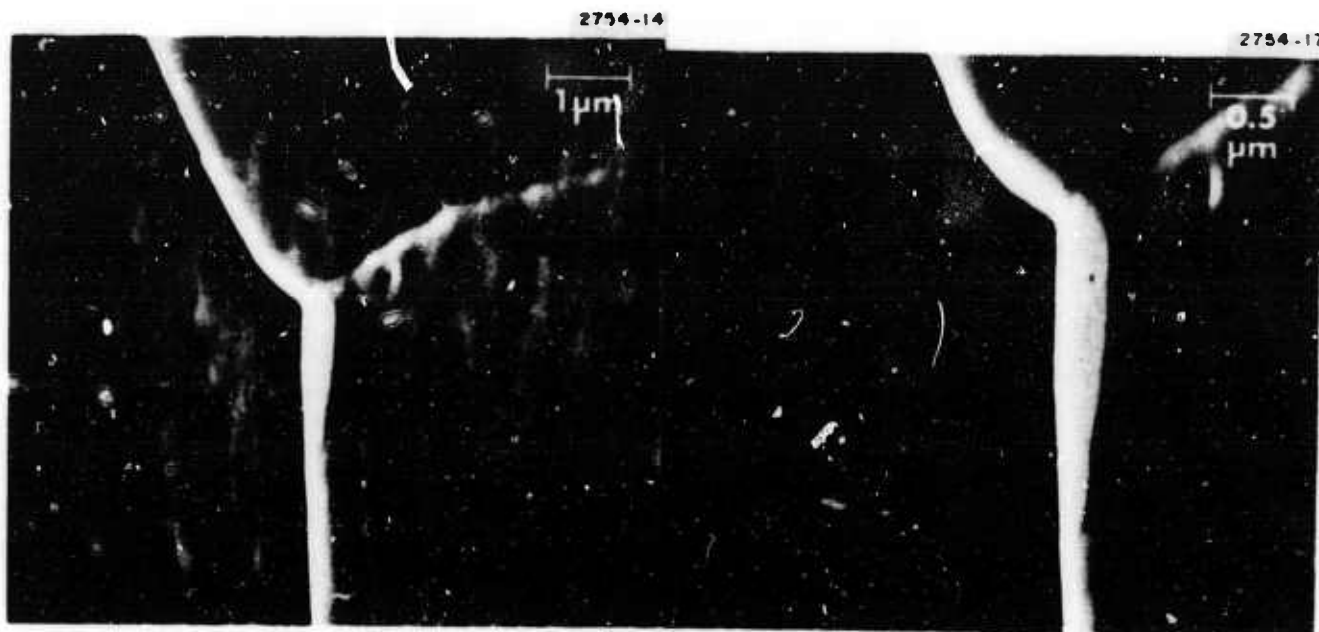


Fig. 5.  
SEM surface topography of KCl sur-  
face mechanically polished and etched  
in HCl (15,000x).



BEAM  $\approx 70^\circ$  TO SURFACE

Fig. 6. SEM photographs of KCl surface at a beam voltage of 20 kV.



using mechanical surface polishing procedures. Initial scans on a Beckman IR 12 spectrophotometer showed several absorption bands, some of which could be attributed to hydrocarbon C-H stretch absorptions. Hydrogen chloride etching for 50 sec removed all but one of the absorption bands and a remaining absorption seen at  $8.2 \mu\text{m}$  is believed to be characteristic of the ATR attachment to the Beckman.

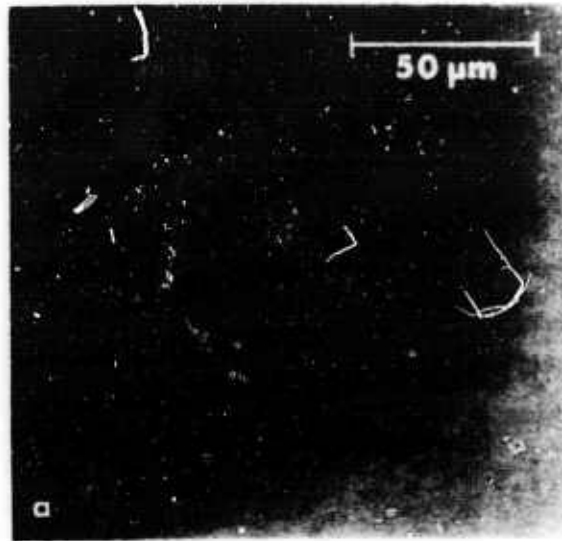
Later work was performed to determine the etch rate under standardized conditions and to improve rinsing and drying conditions. Improved rinsing and drying were accomplished by using Freon TF vapor degreasing as a last step in the etching procedures, and changing the first rinse from ethanol to isopropyl alcohol. This resulted in more reproducible and cleaner finished surfaces.

Figure 7(a) and 7(b) show some results obtained for HCl etching of two press-forged KCl samples. One had been forged some time prior to the experiments (2-20-73) and the second shown in view (b) was forged just prior to etching (10-31-73). These results indicate that the recrystallization induced by forging of undoped halides (to provide increased strength to the material) under the circumstances of the forging conditions used here did not result in a stable crystal structure. Upon aging, the sample produced earlier had reverted to a predominately larger grained single crystal structure. The forging conditions used for the two samples which were pressed from starting blanks 1 in. thick were

2-20-73 was deformed in two steps, 60% at  $200^{\circ}\text{C}$  and 15% further at  $150^{\circ}\text{C}$  at a strain rate of  $0.050 \text{ in. min}^{-1}/\text{in. of remaining length}$ .

10-31-73 was deformed 72% at  $150^{\circ}\text{C}$  at a strain rate of  $0.050 \text{ in. min}^{-1}/\text{in. of remaining length}$ .

The final pressure for the above two samples was 4000 psi; sample 2-20-73 when first forged evidenced a grain size of  $1 \mu\text{m}$  to  $10 \mu\text{m}$  after forging. Measurements made on the same piece 10-19-73 showed very large grains (several mm) with some small areas of 1 to  $10 \mu\text{m}$  crystallites. Sample 10-31-73, when measured after HCl



2754-19

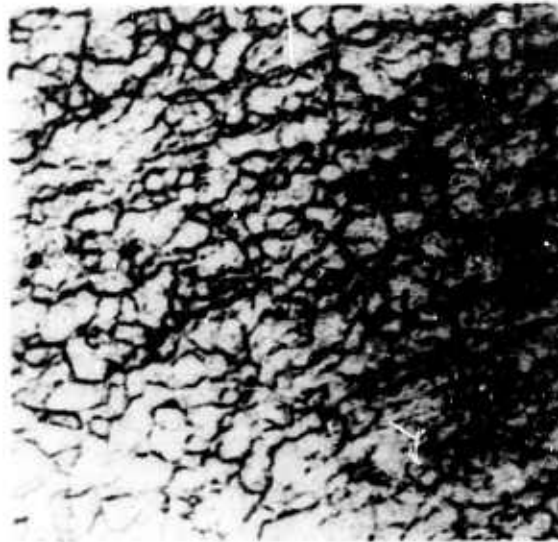


Fig. 7.  
Optical micrographs of press-forged  
KCl after 1 min HCl etch.

surface etching of the forging, indicated material with 1 to 10  $\mu\text{m}$  grain size over the entire surface as shown in Fig. 7(b). Both samples were HCl etched for 1 min.

Further work on the characterization of etched KCl surfaces, and the measurement of pulsed  $\text{CO}_2$  laser damage thresholds for the bulk and the surfaces of single crystal and press forged KCl was reported at the 1974 Symposium on Damage in Laser Materials. The text of the paper is included in the appendix.

## 2. ZnSe Finishing

Surface finishing of zinc selenide for use as an infrared window for some laser system applications requires flatness to within  $\lambda/20$  at 10.6  $\mu\text{m}$  and parallelism to 20 sec of arc. In our work we have been able to meet these requirements using mechanical optical grinding and polishing techniques. These involve grinding the window blanks flat on cast iron laps using  $\text{Al}_2\text{O}_3$  abrasives, followed by final polishing on pitch laps with fine alumina, still retaining flatness and parallelism.

Optical examination of surfaces of ZnSe, finished in the above manner, under bright-field illumination reveals some scratches plus surface digs, resulting from surface pullout caused by the mechanical finishing operations. Further examination of the surface using transmitted light with phase contrast optical equipment reveals a multitude of scratches. We interpret these to be subsurface scratches, since they are not visible using brightfield or darkfield illumination. In addition to these subsurface scratches, one can see a faintly-revealed twinned-grain structure. Phase contrast examination reveals differences in refractive index, so scratches and twinned structure are visible as a result of index changes caused by strain or rearrangement of crystalline structure.

Mechanical removal of surface material by scraping with a metal blade revealed the well-defined twinned structure as seen in the photograph, Fig. 8(a), at 325x magnification. This has led us to deduce the following:

2754-21

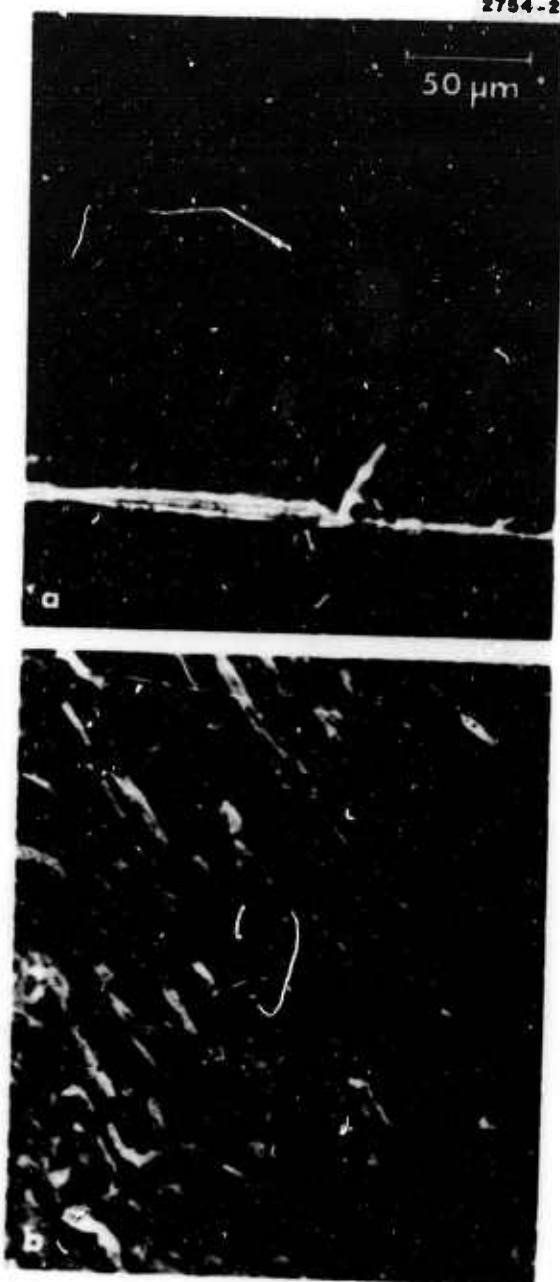


Fig. 8.  
Photomicrographs of ZnSe sur-  
faces after removal of polished  
surface layer (325x).

- a. The mechanically polished ZnSe surface layer is softer than the underlying crystalline substrate.
- b. The surface layer is caused by smearing of the surface during lapping in the near-final polishing stages, since scratches are positioned within the layer and result from the finer abrasives.
- c. We have estimated that the surface layer is thin, about 5000 Å, and amorphous, since no structure is seen in the layer itself.

Removal of most of the surface layer of the ZnSe has been accomplished in our preliminary work by metallographic polishing (fine alumina on a slow fine-cotton lap) as shown in Fig. 8(b). Our efforts to remove this smeared layer were based on our belief that removal of this layer would reduce surface optical absorption at 10.6  $\mu\text{m}$  and contribute to the application of better adhering optical coatings to the ZnSe surfaces.

In view of the high free-energy of the smeared polished layer, we have assumed that rate of attack by a chemical etchant should be sufficiently greater than that of the crystalline subsurface, so that a combination etch-polish technique should give a crystalline surface free of distortion and representative of the bulk material, thus leading to reduced 10.6  $\mu\text{m}$  absorption at the surface.

Our efforts have led to the development of the mechanical-chemical etch-polish finishing procedure for ZnSe outlined below.

#### ZnSe Etch Polish Procedure

1. Grind: Flat and parallel using  $\text{Al}_2\text{O}_3$  microgrit (5 to 9  $\mu\text{m}$  particle size) on a cast iron lap. Starting with 9  $\mu\text{m}$  and ending with 5  $\mu\text{m}$  grit.
2. Polish: Pitch lap using Linde A abrasive, 3 to 4 hours polishing time to remove surface digs and pits.
3. Wash: Clean polished surface in warm  $\text{H}_2\text{O}$  to remove all traces of abrasives.

4. Etch: Immediately, 2 min etch polish after step (3) using alkaline  $K_3Fe(CN)_6$ . \*
5. Clean: Use soap solution (ORVUS), rinse in warm  $H_2O$ .
6. Rinse: Rinse and dry using pure ethanol.

Figure 9(a) shows a 325x photograph of a mechanically polished ZnSe surface using steps (1) and (2) outlined above. Figure 9(b) shows a 325x photograph of the same ZnSe surface after final etch polishing. The crystalline grain structure of the ZnSe can be clearly observed. (The ZnSe used in our work was CVD material produced by Raytheon Corporation.) Using the complete step-wise procedure outlined above we have been able to reproducibly produce polished ZnSe windows that have less than  $0.002\text{ cm}^{-1}$  optical absorption at  $10.6\text{ }\mu\text{m}$ . Using windows polished this way, antireflection coatings can be applied to the window surfaces that meet program goals for an AFML sponsored program reported by M. Braunstein, et al., in the Proceedings, Third Conference on High Power Infrared Laser Window Materials. (Program goal was to produce coated windows that had less than 0.1% reflectance and absorptance at  $10.6\text{ }\mu\text{m}$ .)

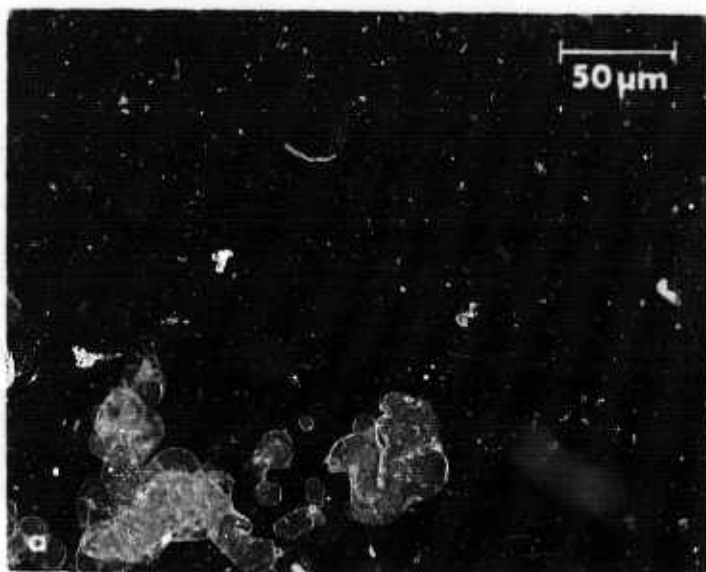
### 3. Ion Polishing of ZnSe

It is well known that mechanical polishing can induce damage in the surfaces of semiconductor materials. Acceptable surfaces should only contain crystal flaws such as dislocations and inclusions that are characteristic of the bulk material and are not artifacts of the processing steps themselves. Sawing, abrasive lapping, polishing and mere handling can induce damage in materials. The degree to which mechanical polishing can damage laser materials in general is not completely known or understood, but our results on the effects of ion beam polishing of ZnSe show that under a restricted range of

---

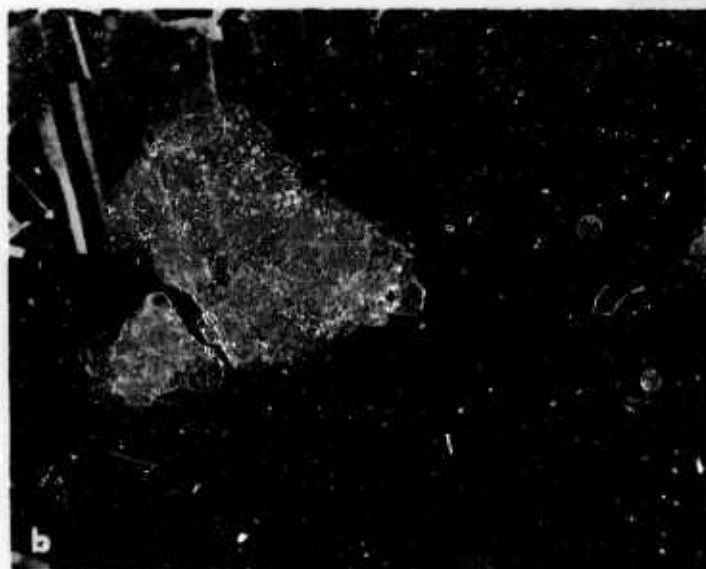
\* $K_3Fe(CN)_6$ , 90 grams; KOH, 1.7 grams;  $H_2O$ , 300 grams.





Mechanical polish

2754-2



Mechanical/chemical  
polish

Fig. 9. Photomicrographs of ZnSe surfaces after mechanical polishing and after final etch polishing (325x).

conditions surface optical absorption and surface optical scattering at  $10.6 \mu\text{m}$  can be reduced below the level that exists right after the ZnSe surface has received its final mechanical polish.

In one ion polishing experiment, for example, a ZnSe window blank that had its surface mechanically polished had an apparent  $\alpha$  at  $10.6 \mu\text{m}$  of  $0.0069 \text{ cm}^{-1}$ ; the same blank after having its surface ion polished with argon for a short time period had an apparent  $\alpha$  reduced to  $0.0044 \text{ cm}^{-1}$ . After continuing the ion polishing for a longer time period the apparent  $\alpha$  of the blank increased to  $0.0110 \text{ cm}^{-1}$ . During this same ion polishing sequence the final optical scattering at  $10.6 \mu\text{m}$  increased tenfold over the value that existed right after mechanical polishing.

We have not yet established the optimum conditions for ion beam surface treatment for ZnSe. The parameters that have to be varied and controlled to standardize the process for optimization of the technique are: sample rotation, angle of argon ion sputtering beam to the blank surface, ion beam energy, ion current density, and time of ion etching. It is clear, however, from the reduction in the surface optical absorption achieved in the initial stages of ion surface bombardment that a continued investigation of ion polishing techniques is warranted.

## B. Surface and Chemical Characterization

### 1. Rutherford Backscattering and Ion Channeling Analyses

a. Polishing Damage in KCl — The energy spectra of Rutherford backscattered light ions, ( $\text{H}^+$  and  $\text{He}^{++}$ ), which are incident in a random direction and along a major channeling axis of a target crystal, provide quantitative information with respect to both the amount and depth distribution of lattice disorder. Such measurements have been especially useful for the study of ion-implantation-produced disorder in Si (Hart and Davies<sup>5</sup>). We have extended this technique to the study of polishing damage in KCl single crystals.

The experimental arrangement is illustrated in Fig. 10. Backscattered particles are detected at an angle of  $160^\circ$  with respect to the incident beam using a cooled Si detector (full width at half maximum  $\sim 5$  keV for  $H^+$ ). The sample is mounted on a goniometer to permit either  $\langle 100 \rangle$  or random alignment of the crystal with respect to the incident beam. An oven assembly which encloses the sample holder permits in situ anneals. A biased W filament may be used to provide electron flooding of the target when necessary to prevent beam charging effects.

The samples used for this work were single crystal platelets of KCl (Optovac) which were cleaved along  $\{100\}$  planes and then polished with either Linde A or Linde B abrasive on flannel using methanol. Backscattered energy spectra of 140 keV  $H^+$  incident in random and  $\langle 100 \rangle$  directions before and after 30 min anneal at  $300^\circ\text{C}$  on a Linde B polished sample are shown in Fig. 11. In this case, a 200 Å carbon layer was deposited on the specimen to prevent beam charging. Before anneal the coincidence of the  $\langle 100 \rangle$  and random yields from the surface to a depth of about 1500 Å indicates that an amorphous layer was formed to this depth by the mechanical polishing. At deeper depths (smaller channel numbers), the  $\langle 100 \rangle$  yield is less than the random yield as a result of ion channeling in at least partially crystalline material. However, long range disorder or strain is suggested since, even though the beam is significantly dechanneled in traversing the amorphous layer, the  $\langle 100 \rangle$  yield does not decrease as much as expected if the substrata were perfectly crystalline below the amorphous layer. The small peaks near channel 70 are caused by the carbon coating. A  $\langle 100 \rangle$  backscattered energy spectrum taken after the anneal sequence is also shown in Fig. 11. As can be seen, the  $\langle 100 \rangle$  yield is about one-half of the random yield, indicating about 50% recrystallization of the amorphous layer and thus comparable ion channeling. Clearly, either longer times or higher anneal temperatures are required to effect complete recrystallization. Nevertheless, the data of Fig. 11 indicate that significant reduction in polishing damage occurs after relatively mild thermal treatment.

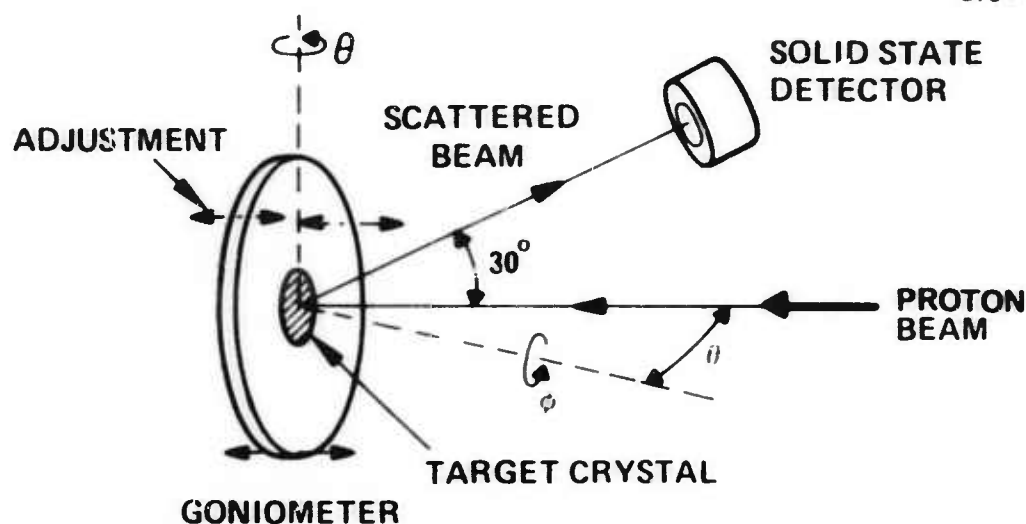
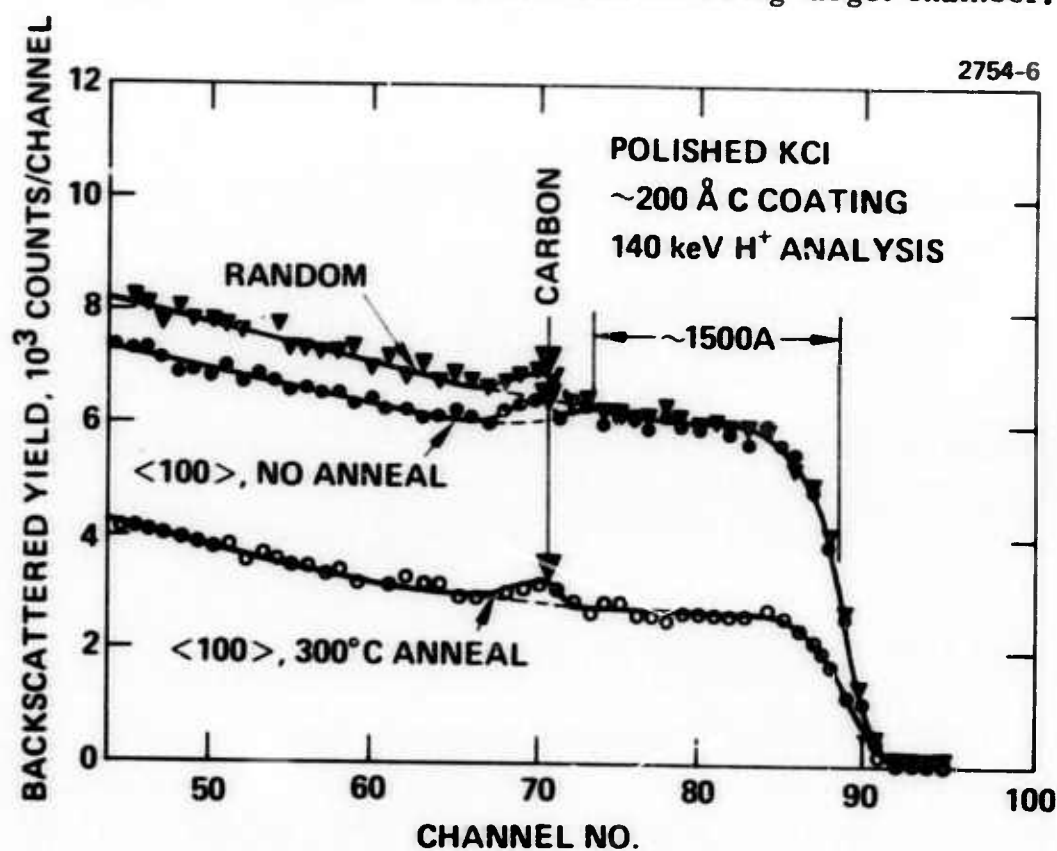


Fig. 10. Schematic of ion backscattering target chamber.



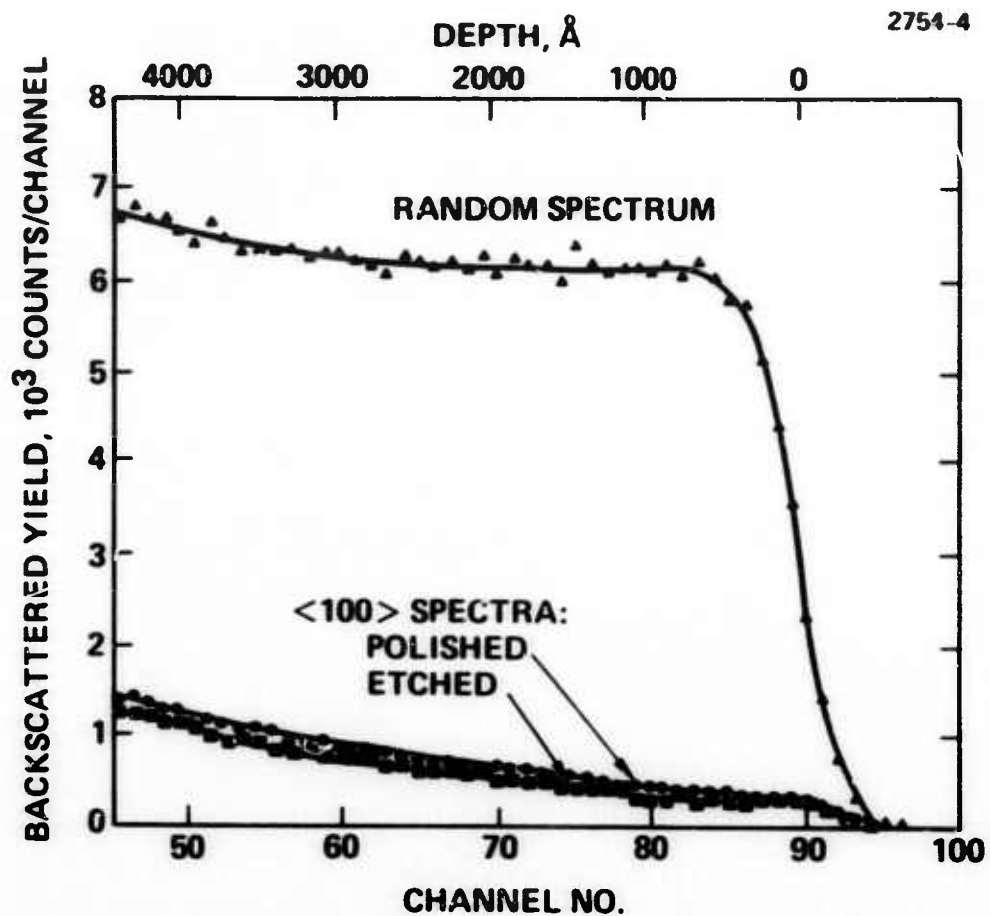
ANALYSIS ION:  $H^+$  AT 140 keV  
 POLISH: LINDE B - METHANOL ON FLANNEL  
 ANNEAL: 30 min AT  $10^{-6}$  Torr

Fig. 11. 140 keV  $H^+$  channeling analysis of polished KCl before and after 300°C anneal.

Backscattered energy spectra of 140 keV  $H^+$  from both a Linde A polished sample and a sample etched for 30 sec in HCl are shown in Fig. 12. In these cases electron flooding prevented beam charging. As can be seen in Fig. 12, the  $\langle 100 \rangle$  backscattered yield of the etched sample near its surface is about 1/20 of the random yield. Such a ratio is consistent with good crystalline qualities. The small peak at the surface (channel 90) is probably caused by a thin surface oxide. Although the  $\langle 100 \rangle$  yield of the polished sample is somewhat greater than that of the etched sample, indicating some lattice disorder or strain, it is remarkable that no amorphous layer is observed as was seen on the Linde B polished sample of Fig. 11. In fact, greater than 90% of the beam remains channeled in the surface region.

Subsequent attempts to reproduce the 1500 Å amorphous layer by polishing with Linde B abrasive also led to little damage. Furthermore, the presence of a 200 Å carbon coating was found to have negligible effect on lattice disorder. Thus, at this time, we can only conclude that the amount of polishing damage is affected by an unknown variable and may be either very little or completely amorphous. However, the fact that very little polishing damage may be produced suggests that polishing may not always strongly affect the surface perfection of KCl.

b. Degradation of KCl Surfaces -- As discussed above, proton channeling effects can be used to measure the crystalline quality of KCl surfaces. As part of a study to correlate lattice disorder with optical absorption we have used this technique to observe significant degradation of KCl surfaces with time. Backscattered energy spectra of 140 keV protons incident along the  $\langle 100 \rangle$  channel of a KCl sample soon after etching (within 2 days) and after 2 months storage in a vacuum desiccator are shown in Fig. 13. The sample was a single-crystal platelet (Optovac) which was cleaved along a  $\{100\}$  plane, mechanically polished, etched in HCl for 1 min, and then rinsed in ethanol followed by Freon vapor degreasing. A tungsten filament provided electron flooding during the proton bombardment to prevent charge buildup.



**ANALYSIS ION:  $\text{H}^+$  AT 140 keV**

**POLISH:**

**LINDE A - METHANOL ON FLANNEL**

**ETCH:**

**30 sec IN HCl**

Fig. 12. 140 keV  $\text{H}^+$  channeling analysis of polished and etched KCl.



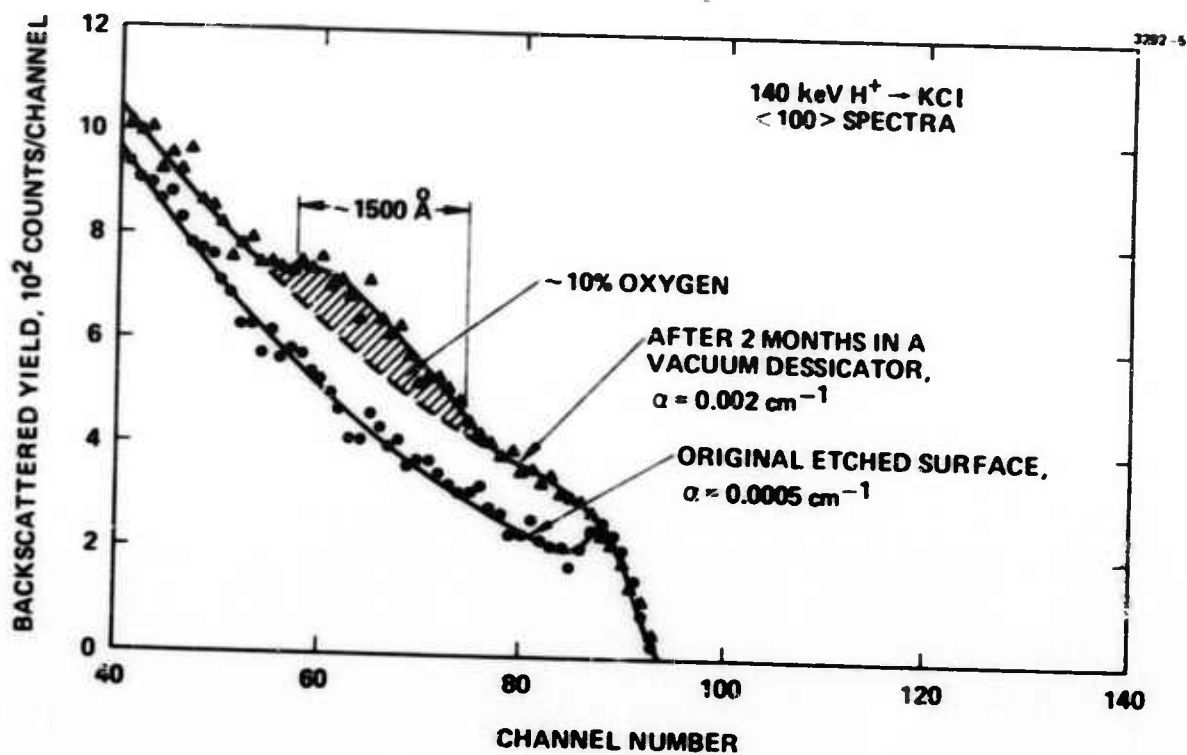
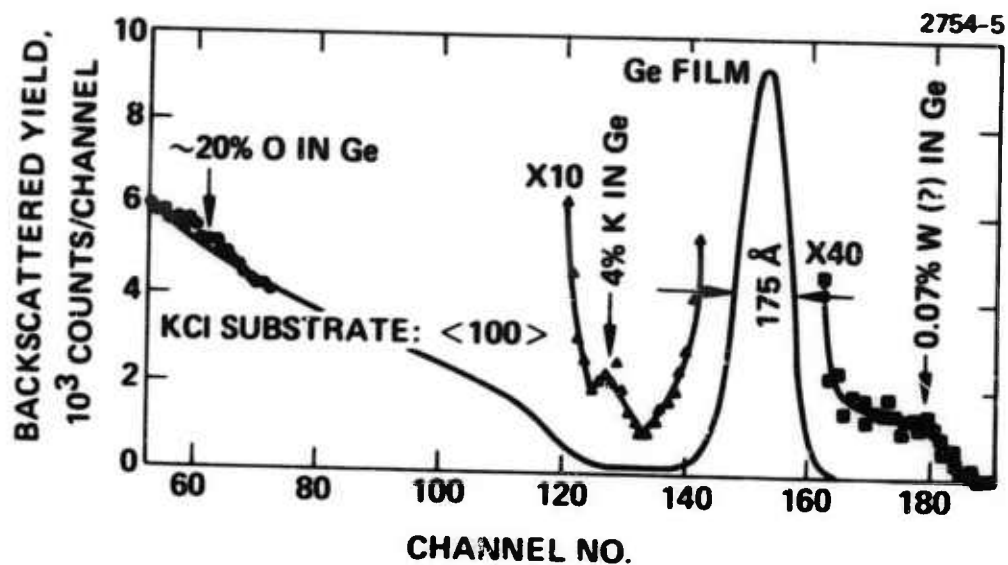


Fig. 13. Backscattered energy spectra of 140 keV protons incident along the 100 channel of KCl after HCl etching and after two months' storage in a vacuum desiccator.

The small peak at the surface (channel 90) of Fig. 13 on the original etched surface is probably caused by a thin oxide layer. The  $\langle 100 \rangle$  yield just behind this peak is about 5% of the random or non-channeled yield, a result typical of a good single crystal surface region. However, the  $\langle 100 \rangle$  spectrum after two months' storage in a vacuum desiccator, which is also shown in Fig. 13 indicates an approximately 50% increase in yield near the surface and a broad peak starting at channel 75. This peak is consistent with the incorporation of about 10% oxygen in a 1500 Å surface layer. The presence of the oxygen apparently causes the increased yield from K and/or Cl atoms near the surface by a distortion of the original lattice. It is also of interest to note that the apparent 10.6 μm absorption coefficient increased from 0.0005 cm<sup>-1</sup> soon after etching to 0.002 cm<sup>-1</sup> after two months' storage. Thus there seems to be a definite correlation of increased absorption with chemical and physical degradation of the surface region. Although additional work is needed to better define the reaction rate of KCl surfaces with environmental conditions, the present results suggest that protective coatings of KCl are essential to long-term surface stability even in a relatively H<sub>2</sub>O-free environment, i.e., a vacuum desiccator.

c. Backscattering Analysis of Germanium Films -

Rutherford backscattering analysis has been used in some preliminary experiments to compare the properties of Ge films on KCl produced in ultrahigh vacuum (UHV) and by ion beam sputtering. Figures 14 and 15 show the results of a comparison of UHV-prepared thin Ge films deposited on KCl at a low rate and a somewhat higher rate, 0.6 Å/sec and 27 Å/sec, respectively. A 2700 Å film deposited at the low rate has a 10.6 μm absorption coefficient of 94 cm<sup>-1</sup> and the more rapidly deposited film with a thickness of 8800 Å has a lower absorption of 24 cm<sup>-1</sup>. The backscattered energy spectra also reveal, when compared, that there is some evidence for presence of heavy metal impurity oxygen and potassium. The concentration of these impurities is somewhat lower in the data shown in Fig. 15 for the



ANALYSIS ION:  $\text{He}^{++}$  AT 280 keV

SAMPLE 8-21-73 U

DEPOSITION CONDITIONS:

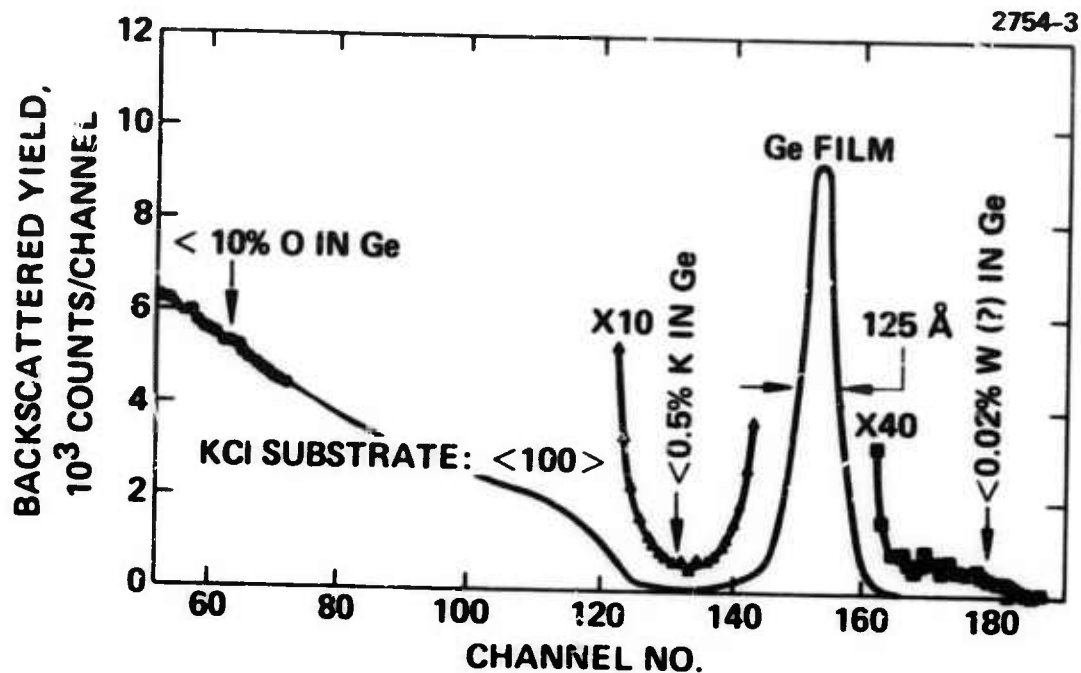
RATE: 0.6 Å/sec

PRESSURE:  $8 \times 10^{-10}$  Torr

SUBSTRATE TEMP.: 150°C

2700 Å Ge ON KCl,  $\alpha = 94 \text{ cm}^{-1}$

Fig. 14. Backscattered energy spectrum of 280 keV  $\text{He}^{++}$  incident on a 175 Å UHV deposited Ge film on KCl.



ANALYSIS ION: He<sup>++</sup> AT 280 keV

SAMPLE 9-25-73 U

DEPOSITION CONDITIONS:

RATE: 27 Å/sec

PRESSURE: 2X10<sup>-8</sup> Torr

SUBSTRATE TEMP.: 150°C

8800 Å Ge ON KCl,  $\alpha = 24 \text{ cm}^{-1}$

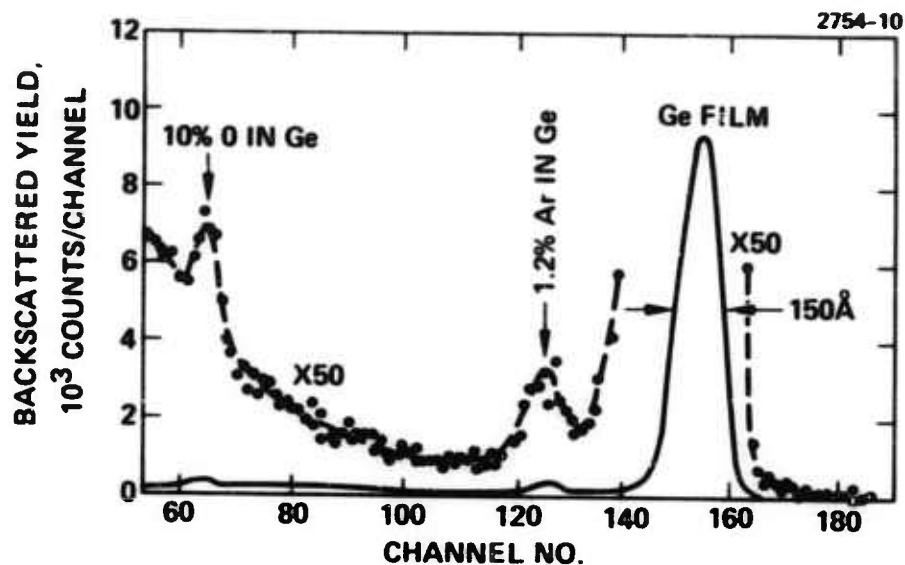
Fig. 15. Backscattered energy spectrum of 280 keV He<sup>++</sup> incident on a 125 Å UHV deposited Ge film on KCl.

more rapidly deposited Ge film. The most surprising result of the analysis of these films has been the presence of the potassium which diffuses into the Ge film from the substrate. The potassium content has been shown to have no influence on the optical absorption properties of the Ge films.

Figure 16 shows the backscattering energy spectrum for a Ge film produced by ion beam sputtering onto a carbon substrate. The carbon substrate was used to allow increased sensitivity for the analysis of oxygen content in the film. In previous experiments we have determined that the carbon support structure had an oxygen level very much reduced below that shown in the data of Fig. 16. The spectrum shown indicates the presence of 1.2% argon and 10% oxygen in the Ge film. A 6000 Å Ge film produced on KCl during the same ion sputtering deposition had an optical absorption coefficient at 10.6 μm of  $36 \pm 12 \text{ cm}^{-1}$ .

Auger electron analysis of the Ge film produced in UHV at the low rate of 0.6 Å/sec was performed to determine if the potassium found in the film using ion backscattering analysis would be confirmed by Auger analysis. As can be seen in Fig. 17, the Auger spectra produced by ion beam sputter profile analysis provide further evidence that the Ge film deposited on KCl has undergone diffusion of the substrate material into the film, as evidenced by the Cl and K peaks.

In Fig. 18 electron microprobe analysis of UHV deposited Ge on KCl is shown for a Ge film produced by T. Donovan of the Naval Weapons Center, China Lake. The 10.6 μm absorption coefficient for this film was measured at HRL to be  $77 \text{ cm}^{-1}$ . The probe analysis showed the presence of K, Cl, and Cu impurities in the film at 0.8%, 0.9%, and 0.4% levels, respectively. It should be noted that the relatively high,  $77 \text{ cm}^{-1}$  value, for the Ge film absorption occurs for a rate of deposition which is low compared with the data for our film shown in Fig. 15, which was 27 Å/sec. This trend for Ge films showing high absorption when produced at low rates is consistent for films produced in oil-pumped vacuum systems too, as will be shown by Ge film data presented later in this report.



ANALYSIS ION:  $\text{He}^{++}$  AT 280 keV

DEPOSITION CONDITIONS:

RATE: 0.5 Å/sec

ION:  $\text{Ar}^+$  AT 7.5 keV

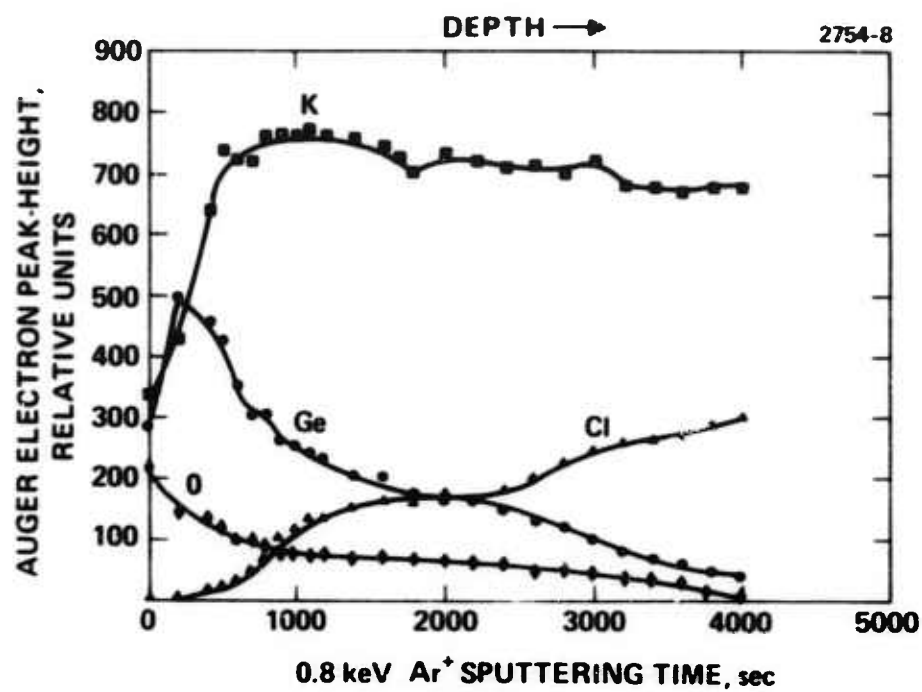
PRESSURE:  $2 \times 10^{-5}$  Torr (Ar),  $5 \times 10^{-7}$  Torr (BASE)

SUBSTRATE TEMP.: 80°C

6000 Å Ge ON KCl,  $\alpha = 36 \pm 12 \text{ cm}^{-1}$

Fig. 16. Backscattered energy spectrum of 280 keV  $\text{H}^{++}$  incident on a 150 Å Ge film sputter deposited onto a carbon substrate.





SAMPLE 8-21-73 U

DEPOSITION CONDITIONS:

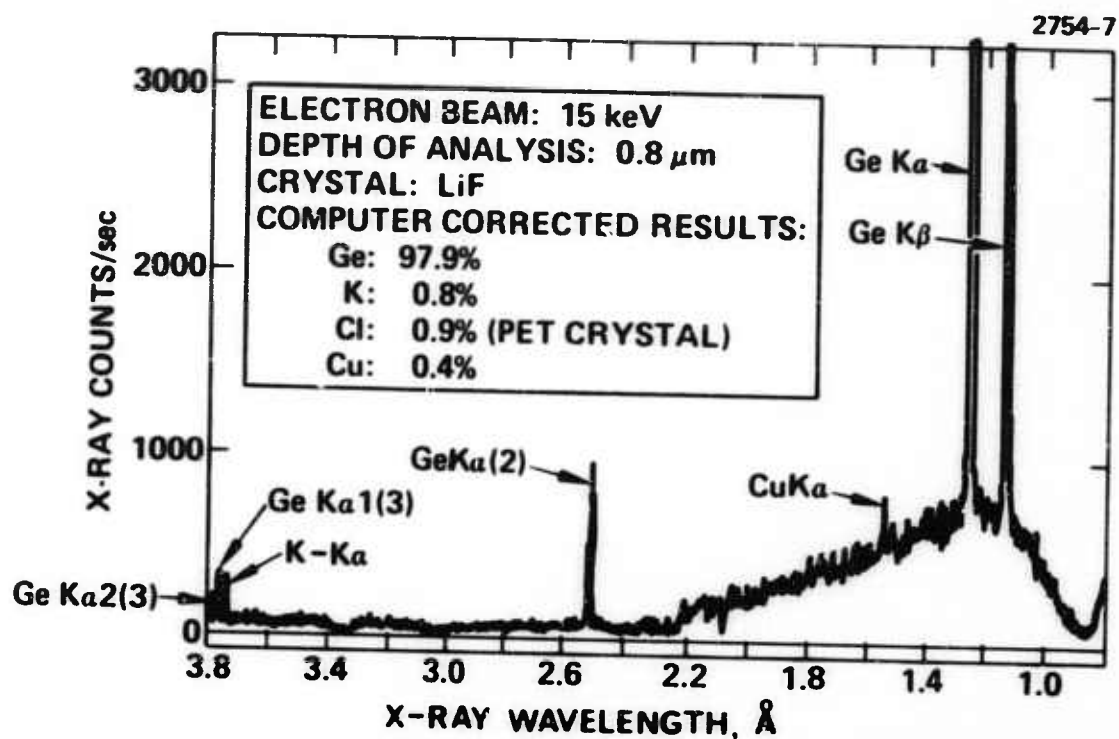
RATE: 0.6 Å/sec

PRESSURE:  $8 \times 10^{-10}$  Torr

SUBSTRATE TEMP.: 150°C

2700 Å Ge On KCl,  $\alpha = 94 \text{ cm}^{-1}$

Fig. 17. Auger electron analysis of a 175 Å UHV deposited Ge film on KCl.



**SAMPLE: DONOVAN #1**  
**DEPOSITION CONDITIONS:**  
 RATE: 1-3  $\text{\AA}/\text{sec.}$   
 PRESSURE:  $1 \times 10^{-9}$  Torr  
 SUBSTRATE TEMP.: AMBIENT  
 ANNEAL: 100°C FOR 2 hr  
 THICKNESS; 1.24  $\mu\text{m}$   
 $\alpha = 77 \text{ cm}^{-1}$

Fig. 18. Electron microprobe analysis of a 1.25  $\mu\text{m}$  UHV deposited Ge film on KCl. Film produced at Naval Weapons Center, China Lake.

Our first analytical data for germanium films deposited on KCl substrates maintained at 150°C during deposition in our ultrahigh vacuum system showed that they contained a heavy element, K, and O impurities. The amounts of these impurities were larger at a slow deposition rate (0.6 Å/sec) than at a fast deposition rate (27 Å/sec). To determine the effect of substrate temperature on the amounts of these impurities, a germanium film was deposited at a low rate (0.17 Å/sec) onto a KCl substrate maintained at 30°C. We were particularly interested in determining whether a lower substrate temperature would reduce the amount of K which diffuses into the germanium film from the KCl substrate.

A backscattered energy spectrum using 280 keV He<sup>++</sup> analysis of this germanium film is shown in Fig. 19. The amounts of K and O in the film are less than the measurement sensitivities, ~1% and ~10%, respectively. These results should be contrasted with the 4% K and 20% O observed earlier in the low rate film deposited at 150°C. Therefore, a reduction of substrate temperature to 30°C markedly reduces the K and O contents in germanium films on KCl.

However, the heavy impurity peak at channel 185 of Fig. 19 is comparable in amount to the 0.07% observed earlier, and consequently, is unaffected by substrate temperature. Electron microprobe analysis of the surface of the germanium material used for the depositions revealed that trace amounts of gold and barium were located in a small area (100 mil radius) near the tip of the germanium which was locally heated by electron beam bombardment during the depositions.

Thus the heavy element peak of Fig. 19 is attributed to gold and barium. It is postulated that the gold may have been present in the bulk of the germanium and diffused to the tip during e-beam bombardment. To check this point the contaminated tip was lapped away, and another low-rate (0.4 Å/sec) germanium film was deposited on KCl. After lapping, microprobe measurements of the germanium source material indicated that the gold and barium had been removed.

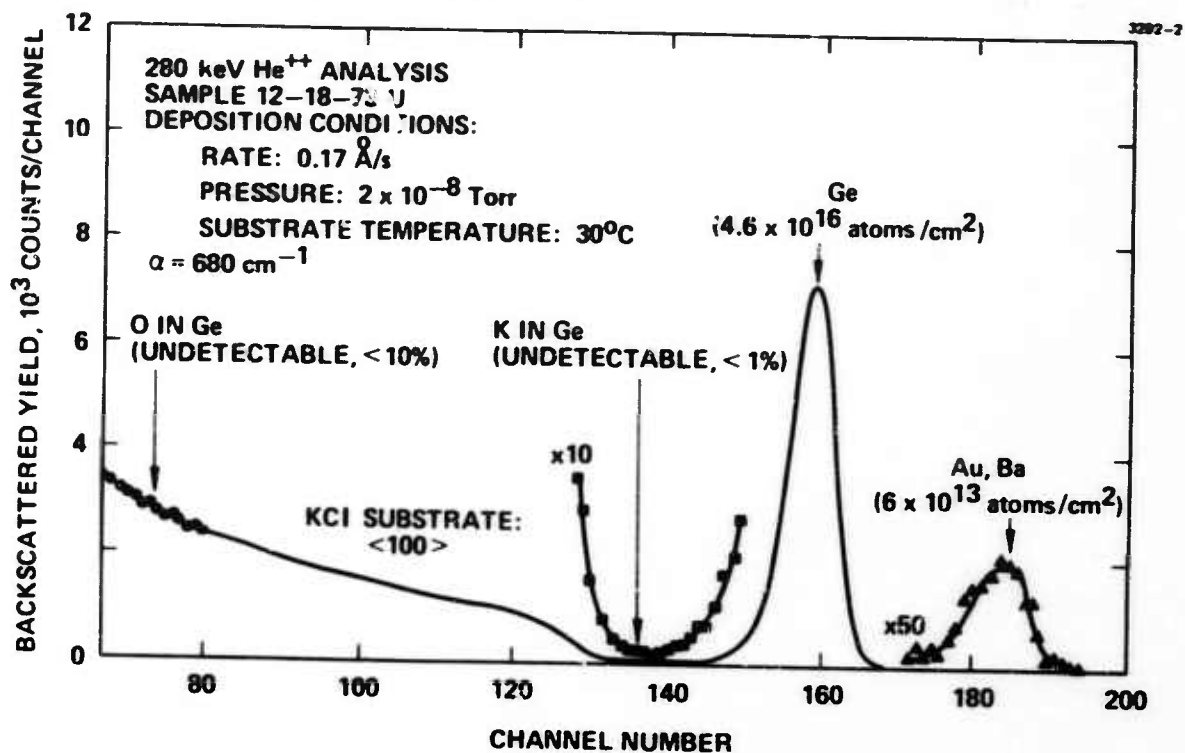


Fig. 19. Backscattered energy spectrum of 280 keV He<sup>++</sup> incident on a thin germanium film evaporated onto KCl in UHV.

A backscattered energy spectrum from this film is shown in Fig. 20. Since the germanium film is much thicker ( $1350 \text{ \AA}$ ) than that of Fig. 19, the heavy impurity peak is broadened. Nevertheless, the level of the backscattered yield from the heavy impurity near the surface at channel 182 of Fig. 20 is reduced to about 0.5 of the previous level. Microprobe analysis of the tip of the germanium source material after evaporation of the film of Fig. 20 revealed that a trace of barium was again present, but that there was no reintroduction of gold. It seems reasonable to attribute the remaining heavy element concentration (0.05%) in the germanium film of Fig. 20 to barium. Since  $\text{BaF}_2$  films were originally deposited in our UHV system, the reintroduction of barium onto the tip of the germanium source material and in the deposited film apparently is caused by residual barium contamination of our vacuum chamber. This result points out the difficulty of avoiding cross contamination of different film materials deposited in the same system.

### C. Coating Techniques

During the course of our program it was our objective to prepare films of materials which might be incorporated in antireflection (AR) coatings for candidate infrared laser window materials by three film preparation techniques: ultrahigh vacuum deposition, ion beam sputtering, and chemical vapor deposition. Using these techniques the films were compared in an effort to determine an optimized method of preparation for use of the films in high energy laser window applications.

#### 1. Ultrahigh Vacuum Film Deposition

a. Germanium Films — The first film material evaluated was germanium. The results for germanium films prepared in UHV have been compared with results for ion sputtered germanium, to prior results for germanium evaporated in conventional vacuum, and to UHV results obtained by T. Donovan at NWC, China Lake. The

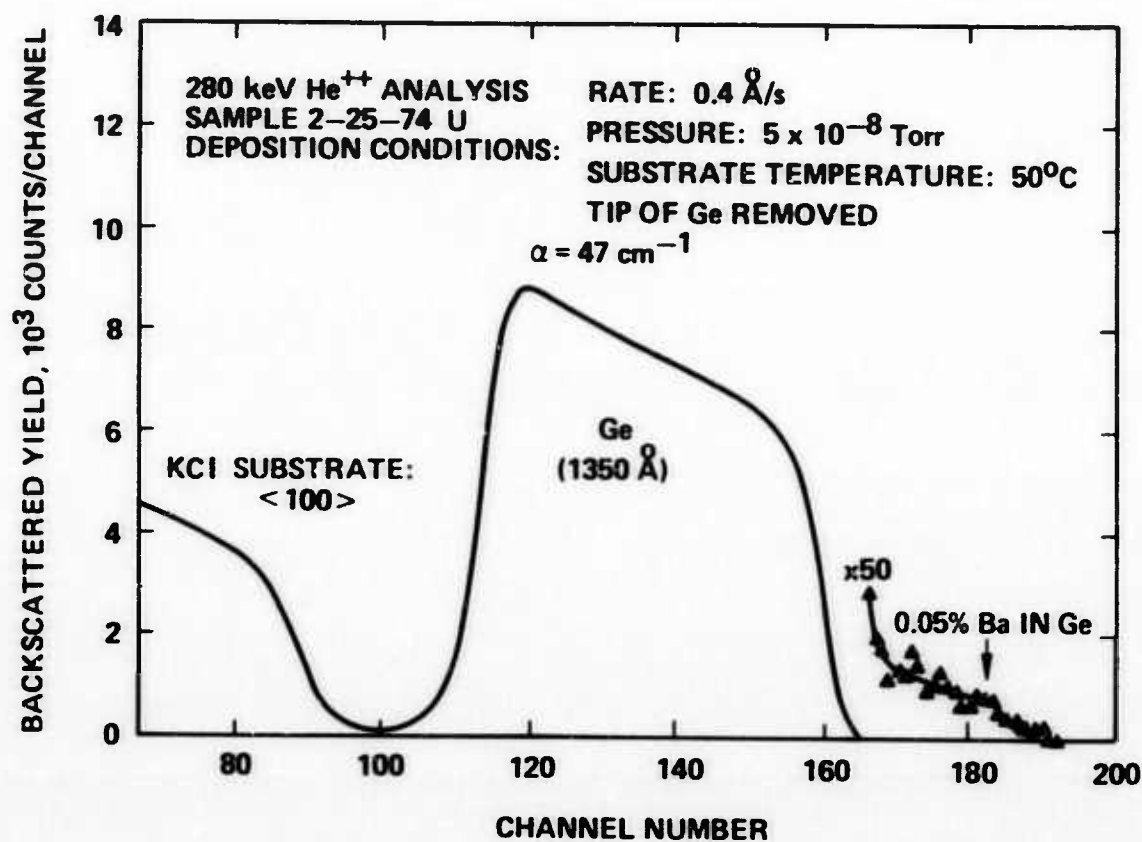


Fig. 20. Backscattered energy spectrum of 280 keV He<sup>++</sup> incident on a 1350 Å germanium film evaporated onto KCl in UHV after removal of the tip of the germanium source material.

prior IIRL results in conventional vacuum showed that e-gun evaporation at high rates was necessary to avoid high absorption at  $10.6\text{ }\mu\text{m}$  which was caused by the tail of a  $13\text{ }\mu\text{m}$  absorption band present in films prepared at low rates of deposition.

The early data are shown in Table 1. The trend shown in the data reported in the table is that lower absorption Ge films are produced at the higher rates of deposition. The germanium film with the lowest absorption,  $10\text{ cm}^{-1}$ , was produced on a ZnSe substrate using ion beam sputtering. A comparable absorption of  $12\text{ cm}^{-1}$  for a film produced on KCl in UHV was obtained at the highest deposition rate of  $70\text{ }\text{\AA}/\text{sec}$  as shown in the table for sample number 7-23-73U. The Ge film prepared by T. Donovan referenced in Fig. 18 had an absorption of  $77\text{ cm}^{-1}$  for a 1 to  $3\text{ }\text{\AA}/\text{sec}$  deposition rate under UHV conditions.

In later work, the inverse dependence of  $10.6\text{ }\mu\text{m}$  absorption on film deposition rate was confirmed. Correlations were found between the deposition rate, the impurity content, and physical structure of the films which appear to explain the results.

Figure 21 summarizes the germanium film absorption versus deposition rate results. The points which fall on the dashed curve are for films of more than a few hundred angstroms in thickness. These points clearly show the inverse dependence of  $10.6\text{ }\mu\text{m}$  absorption on deposition rate. Other deposition parameters, such as substrate temperature and system pressure during deposition, were found not to affect the absorption results within the ranges studied (pressure:  $1.5 \times 10^{-7}$  -  $2.5 \times 10^{-9}$  Torr; temperature 27 to  $150^{\circ}\text{C}$ ). The two points which are labeled " $90\text{ }\text{\AA}$  film" in Fig. 21 are indicative of an excess absorption in thin layers which is probably concentrated at the film-substrate interface. This high apparent absorption coefficient in thin layers is a result of assuming a uniform absorption coefficient throughout the layer and thereby neglecting the possibility of any surface effects. For the thicker layers the error introduced is small since the surface absorption is a small percentage of the total



TABLE I  
Germanium Film Data

Sample Number	Preparation Technique	Pressure During Deposition, Torr	Substrate	Substrate Temperature, °C	Deposition Rate, Å/sec	10.6 μm Absorption, cm <sup>-1</sup>	Comments
B11-9	E-gun in conventional vacuum	$2 \times 10^{-6}$	RAP KCl	100	33	12 to 24	(13 μm absorption)
B24-4	Resistance source in conventional vacuum	$2 \times 10^{-6}$	RAP KCl	50	4 to 5	~10,000	
B-23-13	Ion beam sputtered in conventional vacuum	$2 \times 10^{-5}$ , Ar	RAP KCl	125	2 to 3	24 to 48	
R20	Ion beam sputtered in conventional vacuum	$2 \times 10^{-5}$ , Ar	Raytheon ZnSe	125	2 to 3	10	
7-23-73U	E-gun in UHV	$1.5 \times 10^{-7}$	RAP KCl	Ambient	70	12	
9-25-73U	E-gun in UHV	$2 \times 10^{-8}$	RAP KCl (etched)	150	42	24	
8-21-73U	E-gun in UHV	$2 \times 10^{-9}$	RAP KCl	150	0.8	94	

T1191

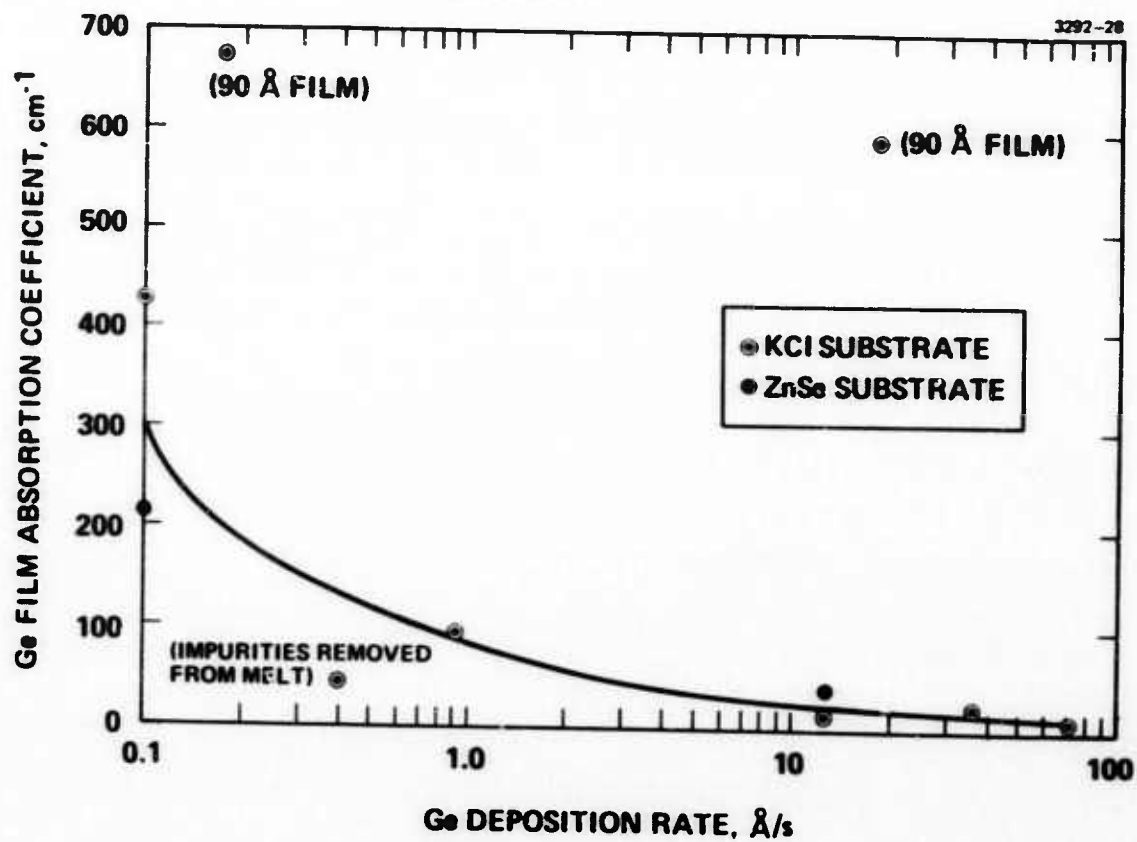


Fig. 21.  $10.6 \mu\text{m}$  absorption versus deposition rate for UHV germanium films.

absorption. It was believed at first that the controlling parameter in the absorption data was the amount of potassium and chlorine interdiffusion between the germanium film and the KCl substrates. This potential explanation was weakened by finding the same rate dependence of absorption on ZnSe substrates as on KCl. It was subsequently found that the interdiffusion was essentially eliminated when the substrate temperature during deposition was reduced from about 150°C to 80°C or less. The rate dependence of absorption did not change at this point; therefore, other explanations were sought. Heavy metal impurities which were detected in the germanium films by Rutherford backscattering were found to be correlated with gold and barium found by electron microprobe analysis in the tip of the germanium source material.

A germanium film prepared after removal of these impurities from the germanium melt had a greatly reduced heavy metal content and had low absorption compared with previous films. A partial explanation of the rate dependence of absorption is provided by these observations. The impurities in the germanium source material were concentrated in the last-to-freeze portion of the conical-shaped melt that develops when the e-gun evaporator is turned off after a run. In subsequent runs at low rates only this tip of the germanium material is melted by the e-gun, and, therefore, the impurity content of the evaporating material is probably high. When a run is made at high deposition rate the entire germanium charge is melted, the impurities are dissolved in a large amount of germanium, and the impurity content of the evaporating material is probably low. The amount of gold which was present at the melt tip is consistent with the gold concentration which would have been used to dope the germanium for high resistivity. The vacuum melting and slow cooling which we have subjected the material to has probably resulted in a zone refining action. (It should be pointed out that the Ge source material was purchased with the condition that it be vacuum zone refined material of 99.999% purity, or better, with respect to metals.) The heavy metal impurities cannot be responsible for the entire rate dependence of the absorption

for a number of reasons. Even after removal of most of the heavy metal contamination there is still an excess absorption of a factor of four for films prepared at low rates over those prepared at high rates. A further confirmation of this excess is the fact that germanium films sputtered at  $0.5 \text{ \AA}/\text{sec}$  were found to have absorptions in the neighborhood of  $10 \text{ cm}^{-1}$ . Therefore, a study of the physical structure of germanium films on KCl and ZnSe substrates was initiated.

X-ray diffractometer scans taken on films on KCl and ZnSe prepared at both high and low rates showed only a broad low angle continuum from the germanium films. This is usually taken to be indicative of an amorphous structure, but is not conclusive for thin films. Reflection electron diffraction observations were done next on the same four samples. The high rate films showed a diffuse low angle scattering, which is again indicative of amorphous structure. In this experiment the low rate films showed well developed debye rings indicative of polycrystalline structure with no preferred orientation. Finally, the films on the KCl substrates were floated free by immersion in water and mounted on copper grids for examination by transmission electron diffraction. The low rate film was found to consist of randomly oriented crystallites with a size equal to or less than the  $100 \text{ \AA}$  electron beam diameter. The high rate film was too thick to transmit the electron beam and, therefore, could not be studied by this method. It is probable, however, that it would have been found to be truly amorphous. These observations provide the probable reason for the remainder of the excess  $10.6 \text{ \mu m}$  absorption in low rate films as an effect of departure from amorphous structure. They support the conclusions as to structural effects on the infrared absorption by germanium films arrived at by T. Donovan (NWC-China Lake) by indirect means.

b. ThF<sub>4</sub> Films — At the conclusion of the work on ultrahigh vacuum deposition of germanium, attention was turned to ThF<sub>4</sub>. The germanium work was useful in learning to deposit and monitor films in the UHV system and in evaluating the usefulness of

the various physical and chemical analytical tools at our disposal. However, it is not expected that germanium will be a usable film material for most high energy laser applications nor is it clear that UHV deposition provides any advantage over conventional vacuum for it. The situation was expected to be different for  $\text{ThF}_4$ . It is the best available low index material for  $10.6\ \mu\text{m}$  use which is not water soluble. Furthermore, in the UHV environment the major residual gas after bakeout is normally hydrogen rather than water as in conventional systems. For a fluoride material whose infrared absorption is strongly affected by oxygen and  $\text{OH}^-$  content the environment in the UHV system should lead to reduced absorption in the films.

In the initial  $\text{ThF}_4$  depositions the water residual was relatively high and the  $\text{ThF}_4$  absorption was similar to that of films prepared in conventional systems. Careful mass spectrographic analysis of residual gases, leak detection, and bakeout testing was initiated in order to be certain that the best possible background conditions was obtained in future depositions.

An extensive series of experiments then showed that the only important variable in controlling the water content, and thus the  $10.6\ \mu\text{m}$  absorption of UHV deposited  $\text{ThF}_4$  films is substrate temperature. This result is the same as in conventional vacuum systems. The minimum absorption coefficients in the films are near  $10\ \text{cm}^{-1}$  in both types of vacuum environment. Details of this work, together with much of the other film data and analytical work were presented at the Fourth Conference on High Power Infrared Laser Window Materials. The text of this paper is included in the appendix.

## 2. Compositions of Fluoride Films

The compositions of several fluoride films were determined during the course of the program. We were especially interested in comparing the compositions of evaporated and sputter-deposited thorium fluoride. A backscattered energy spectrum of  $280\ \text{keV}\ \text{He}^{++}$  from an evaporated thorium fluoride film on a carbon substrate is shown in Fig. 22. The amounts of thorium and fluorine in the film are

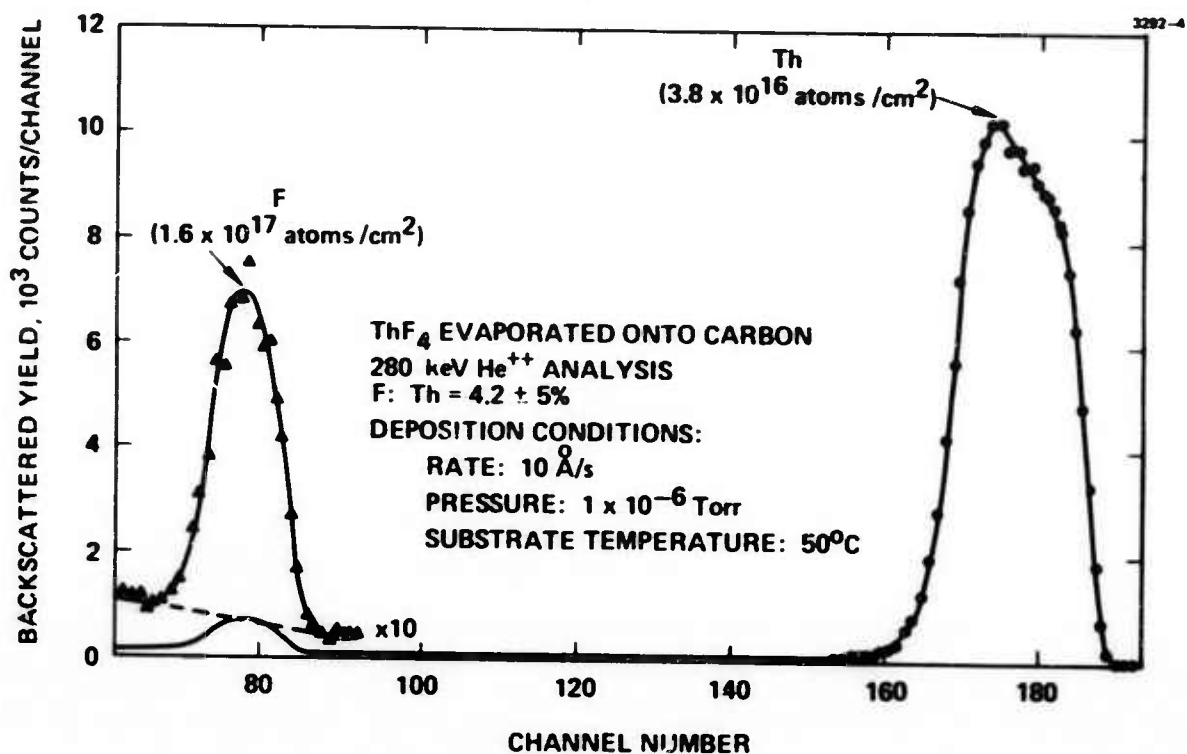


Fig. 22. Backscattered energy spectrum of 280 keV He<sup>++</sup> incident on a ThF<sub>4</sub> film evaporated onto a carbon substrate.

determined from the areas of the peaks corresponding to scattering from thorium and fluorine atoms, respectively, together with the known Rutherford scattering cross sections and are indicated on the figure. The ratio of the number of fluoride atoms to the number of thorium atoms is calculated to be  $4.2 \pm 5\%$ , the estimated error being caused primarily by uncertainty in the background level of the fluoride peak, the dashed line of Fig. 22. Therefore, this ratio of fluoride to thorium is in agreement with the expected composition of  $\text{ThF}_4$ . Furthermore, no impurities were detectable.

The results of similar measurements of  $\text{Ar}^+$  beam sputter-deposited thorium fluoride and magnesium fluoride together with an electron microprobe analysis of rf plasma sputter-deposited thorium fluoride are summarized in Table II. Also included in the table are the results from the evaporated  $\text{ThF}_4$  film discussed above. In all cases the sputter-deposited films were strongly deficient in fluorine. Clearly, normal sputtering procedures are inadequate for the formation of stoichiometric fluoride films. In addition, impurities were detected in the sputter-deposited films as indicated in Table II. It is interesting to note that the source of sodium in the rf plasma-deposited thorium fluoride was traced to the presence of 10% sodium in the sputter target. The  $\text{Fe}(?)$  and  $\text{W}(?)$  impurities apparently come from the structure of the sputter ion gun.

### 3. Chemical Vapor Deposition (CVD)

The primary objectives of this task included the investigation of CVD and physical vapor deposition (PVD) of chalcogenide materials, especially  $\text{As}_2\text{S}_3$ , for the evaluation of these techniques in producing high quality, protective, antireflective coatings on optical materials such as  $\text{KCl}$ ,  $\text{ZnSe}$ , and  $\text{CaF}_2$ .



TABLE II  
Compositions of Fluoride Films

Desired Composition	Deposition Technique	Analysis Technique	Actual Composition	Impurities
ThF <sub>4</sub>	Evaporation	He <sup>++</sup>	ThF <sub>4</sub>	None detected
ThF <sub>4</sub>	Sputtering (rf plasma)	Probe	ThF	4% Na*
ThF <sub>4</sub>	Sputtering (Ar <sup>+</sup> beam)	He <sup>++</sup>	ThF	Ar, Fe(?), W(?)
MgF <sub>2</sub>	Sputtering (Ar <sup>+</sup> beam)	He <sup>++</sup>	MgF	Ar, Fe(?), W(?)
*Electron microprobe analysis of sputter target revealed 10% Na contamination.				

T1396

Early in the program, a number of runs were made using an open tube PVD system (Fig. 23) in which As<sub>2</sub>S<sub>3</sub> was heated in a stream of hot dry nitrogen. The As<sub>2</sub>S<sub>3</sub> had been prepared by direct reaction of the elements which were purchased commercially and evaluated to be 99.9999% pure. The reaction takes place by heating arsenic (which has been previously sublimed) with sulfur in stoichiometric proportions in a sealed evacuated vitreous silica tube. The resulting product As<sub>2</sub>S<sub>3</sub> forms a clear red glass when rapidly cooled.

This material was used as source material in the PVD investigation. Experiments were performed using vitreous silica substrates as well as cleaved or cut and polished KCl surfaces. The series of experiments indicated that a freshly etched surface of KCl was necessary in order to get a smooth film. The result of these experiments was the deposition of films of As<sub>2</sub>S<sub>2</sub>. Because of the difficulties of composition control in this type of apparatus, construction of a CVD apparatus was begun.

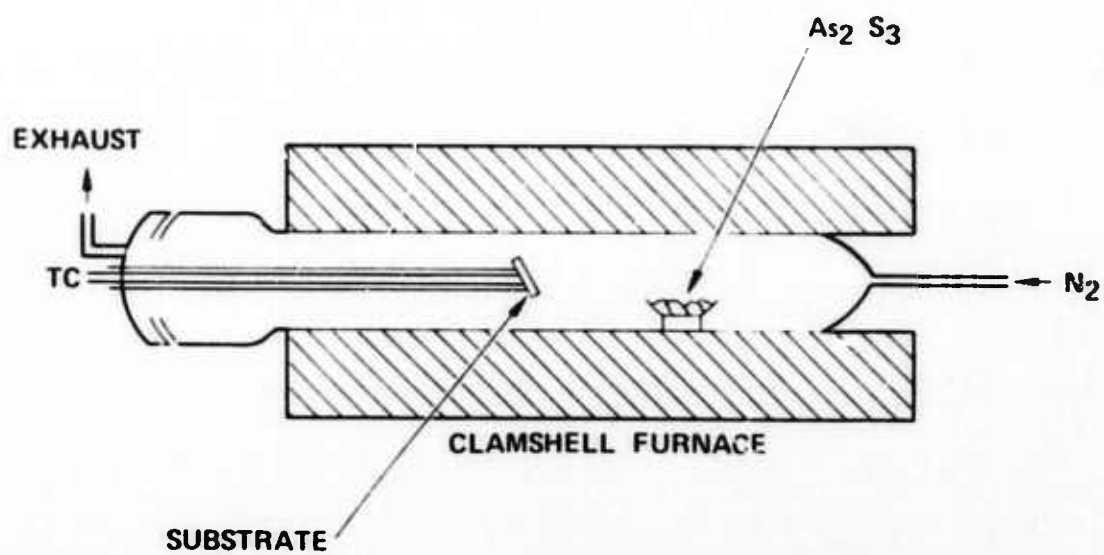


Fig. 23. PVD apparatus.

The CVD apparatus (Figs. 24 and 25) was completed early in 1974. The apparatus is designed for the reaction:



where  $\text{H}_2$  acts as a carrier gas for the  $\text{AsCl}_3$ . A few experimental runs were made on vitreous silica substrates to establish reaction conditions. After these runs, freshly HCl-etched KCl was used. Fifteen runs were made on KCl substrates varying gas flow rates ( $\text{H}_2\text{S}$  and  $\text{H}_2$ ) and substrate temperature. The reaction furnace (furnace 2 in Fig. 24) was maintained at  $650^\circ\text{C}$  to ensure reaction and prevent any deposition in the reaction chamber. The substrate temperature was controlled by furnace 1. Substrate temperatures were monitored by placing a thermocouple directly below the substrate: temperatures were varied from 100 to  $200^\circ\text{C}$ . Flow rates were varied from 10 to 50 standard cc/min for  $\text{H}_2\text{S}$ , and 40 to 220 standard cc/min  $\text{H}_2$ ; rates were adjusted to create stoichiometric conditions in the reaction chamber. Optimum gas flow conditions were obtained at approximately 15 standard cc/min  $\text{H}_2\text{S}$  and 60 standard cc/min  $\text{H}_2$ . More rapid flows caused streaming and uneven deposition on the substrate.

The following results were obtained:

- a. Amorphous films of  $\text{As}_2\text{S}_3$  having good uniformity were grown on KCl substrates, typically the films were less than  $1 \mu\text{m}$  thick.
- b. Composition of the product being deposited can be controlled by adjusting the flow rates of  $\text{H}_2\text{S}$  and  $\text{H}_2$  (carrier gas for  $\text{AsCl}_3$ ).
- c. Quality control of the films is strongly dependent on substrate temperature and gas flow rates; best films have been grown at temperatures of approximately  $150^\circ\text{C}$  (but not at lower temperatures) and gas flow rates of approximately 15 standard cc/min  $\text{H}_2\text{S}$  and 60 standard cc/min  $\text{H}_2$  (but not at higher gas flow rates).

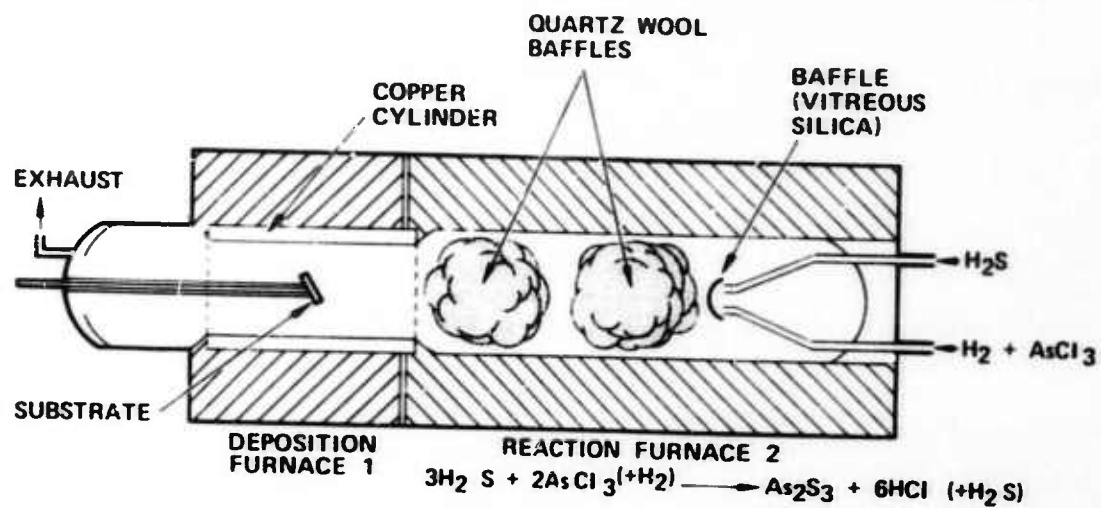


Fig. 24. CVD apparatus.

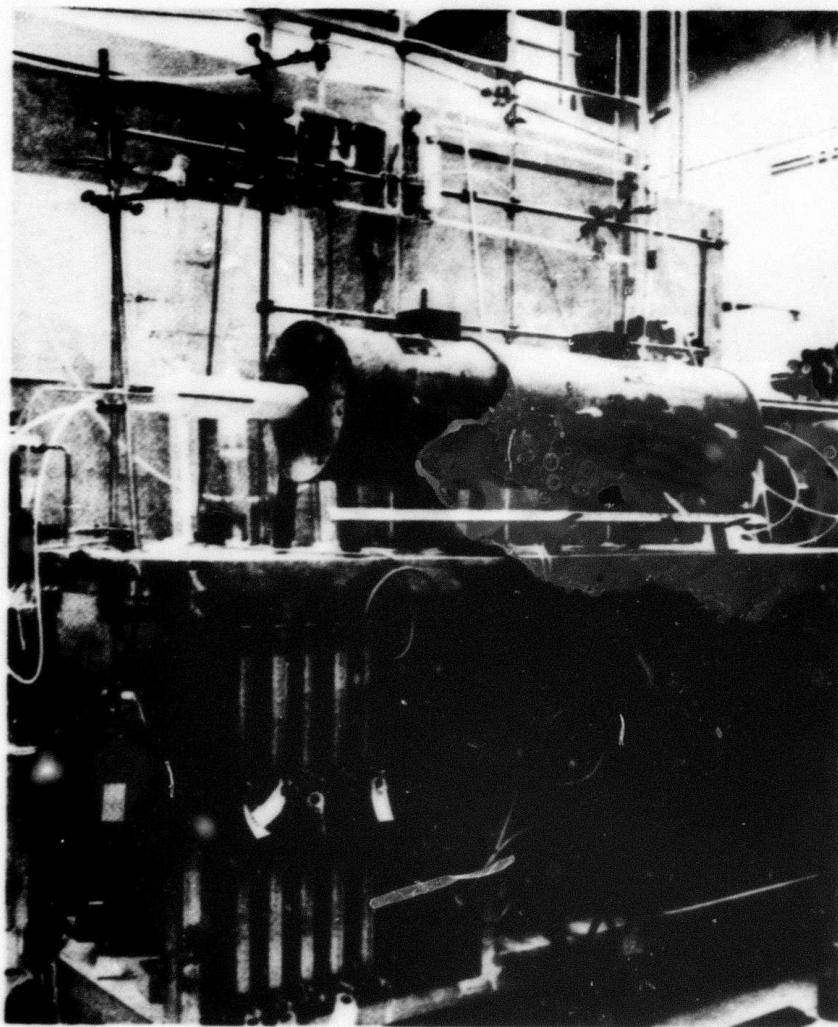


Fig. 25. Chemical vapor deposition of  $\text{As}_2\text{S}_3$ .



- d. Increased temperature of the substrate has indicated an epitaxial growth of  $\text{As}_2\text{S}_3$  on KCl. This was accomplished only once and has not been reproduced.
- e. Crystal surface quality is of utmost importance since any surface flaw (scratch, or crystal defect) will cause spurious crystal nucleation.

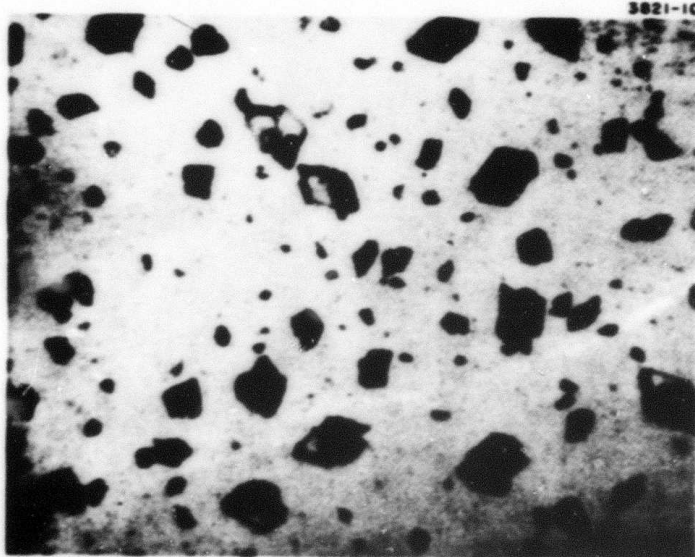
The major problem encountered was the growth of crystals spuriously nucleating on the surface. These crystals have been observed to be surrounded by an amorphous thin film matrix whose composition has been determined to be  $\text{As}_2\text{S}_3$ . The crystals have been made to vary in composition (with variations in gas flow rates) from  $\text{As}_2\text{S}_2$  to  $\text{As}_4\text{S}_3$  (dimorphite) (See Fig. 26). Variations in substrate temperature indicated better crystal morphology at elevated temperatures (180 to 200°C) and more dendritic growth at lower temperatures (150 to 170°C); in either case the larger crystals appeared to grow at the expense of the surrounding smaller ones creating island-like appearances across the  $\text{As}_2\text{S}_3$  matrix (Fig. 27). Figure 27 also shows the tendency for crystal nucleation along surface flaws, especially scratches. An experiment designed to minimize surface nucleation by the initial deposition of an  $\text{As}_2\text{S}_3$  film by vacuum evaporation was performed on KCl substrates. Following HCl etchings, half of the surface was masked and a thin  $\text{As}_2\text{S}_3$  film was deposited. The sample then was loaded into the CVD apparatus and heated to 160°C. After four hours of deposition at optimum rates (see above) the results shown in Fig. 28 were observed. The precoated side (right side of photograph) showed a fairly uniform dendritic growth over the film with islands of larger dendrites, again appearing to grow at the expense of surrounding smaller dendrites. The uncoated side showed less uniform dendritic growth having more islands with some small dendrite regions. A thin film of  $\text{As}_2\text{S}_3$  appears to have grown as well, forming the principal matrix on the uncoated side. Reduction in substrate temperature to below 150°C (approximately 140°C) did not improve the film quality, but caused more uniform deposition of crystallites (Fig. 29) the smaller ones on the precoated side.



3821-9

a. Microprobe SEM photograph.

350X



3821-10

b. Photomicrograph.

320X

Fig. 26. Dimorphite crystals on As<sub>2</sub>S<sub>3</sub> matrix — KCL substrate.



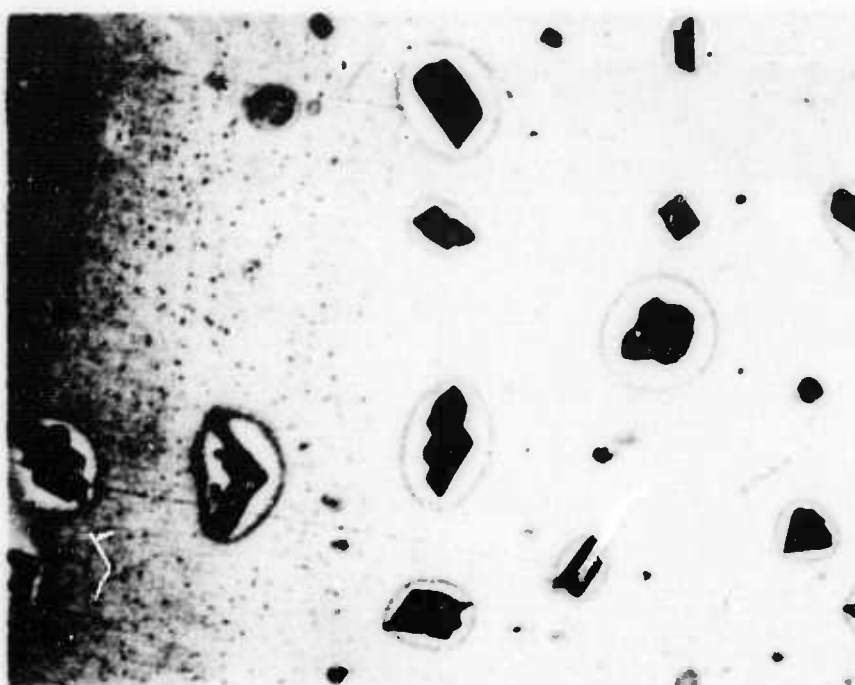


Fig. 27. Crystal "islands" on  $\text{As}_2\text{S}_3$  matrix, KCl substrate (50x).



Fig. 28.  $\text{As}_2\text{S}_3$  deposit on uncoated (left) and pre-coated KCl substrate (50x).

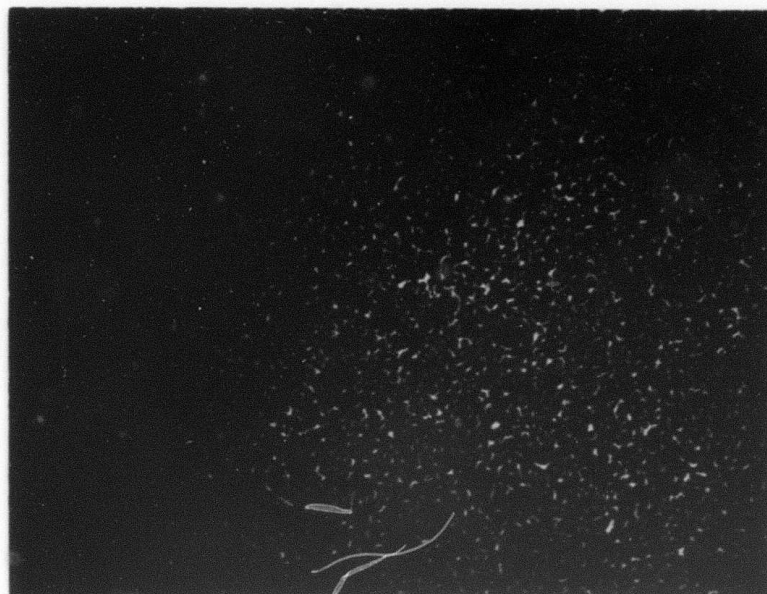


Fig. 29(a). Deposition at low temperature on previously coated KCl (50x).

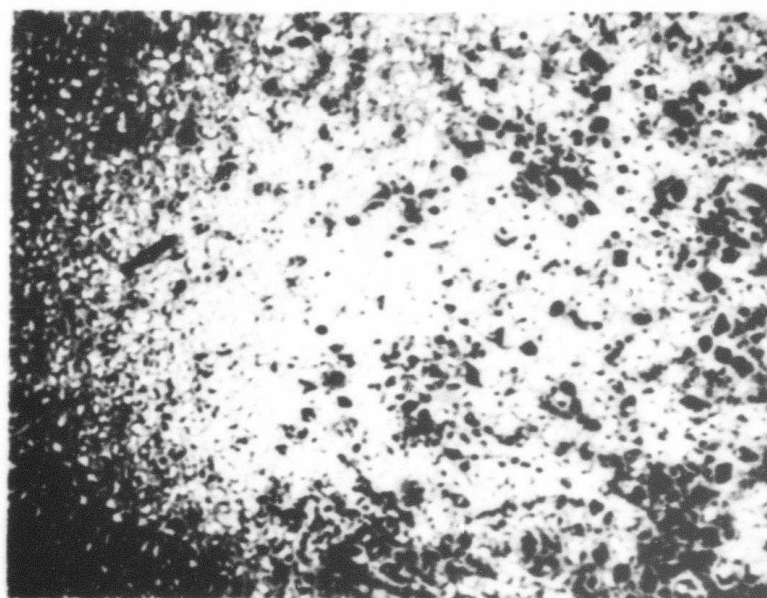


Fig. 29(b). Deposition at lower temperature on uncoated KCl (50x).

The work performed on this program is expected to continue in the follow-on contract beginning January 1975. The most important results from this first study are

- a. The uniform deposition of an amorphous  $\text{As}_2\text{S}_3$  film
- b. The epitaxial growth of arsenic sulfide on KCl.

We plan to pursue perfection of these films as well as investigate other chalcogenides and halide films by the CVD and PVD techniques. We have not achieved the perfect set of conditions for the  $\text{As}_2\text{S}_3$  film deposition, and several experiments will be performed to realize that goal. The importance of surface finishing on the substrate has been clearly established from our experiments and surface preparation will be an important aspect in the continuing effort.

#### D. Optical Evaluation

During the course of our program optical evaluation of windows and coatings was performed using absorption calorimetry, interferometry, polarizing microscopy, spectrophotometry, optical scattering, and ellipsometry. The modulated light ellipsometer which was constructed for use at  $10.6 \mu\text{m}$  is a unique instrument and is therefore described here.

To be able to properly design optical coatings and to be able to interpret experimental results it is necessary to have available good data on the optical constants of the materials involved. This is particularly important for film materials, in which the optical properties may depend on preparation conditions, and for new bulk materials, or in cases where surface or interfacial effects are important.

Such information is most expeditiously obtained by the method of ellipsometry, in which polarized light is incident on the sample and the ratio of the amplitude reflectances for light polarized parallel and perpendicular to the plane of incidence is measured. Such an

instrument was constructed. The HRL ellipsometer differs from conventional instruments in several respects, the most significant being the manner in which the data are extracted and the operating wavelength range. In most conventional ellipsometers the optical train consists of light source, polarizer, quarter wave plate, sample, analyzer, and detector. The usual method of operation is to set the polarizer at  $45^\circ$  and then to adjust the quarter wave plate and analyzer (either manually, or under computer control) in order to extinguish the light falling on the detector. This is a very laborious procedure which requires extreme accuracy in the measurement of the final angles of the components in order to extract the desired optical constants.

The HRL instrument utilizes an acousto-optic modulator in place of the quarter wave plate. The polarizer, modulator, and analyzer optic axes can then be left in fixed positions and the data extracted electronically from the signals at the detector at the first and second harmonic of the modulator drive frequency. This method has the advantages of elimination of a tedious measurement procedure, higher sensitivity for the measurement of small absorptions, and the relaxation of the angular accuracy requirements.

A basic modular ellipsometer system with quartz optics which was purchased from Rudolf Research Corporation will operate in the wavelength region from  $3000 \text{ \AA}$  to approximately  $7000 \text{ \AA}$  with a commercial fused quartz modulator and the standard Rudolf photomultiplier detection system. The addition of an InSb detector will permit operation to approximately  $4 \text{ }\mu\text{m}$ . Also,  $10.6 \text{ }\mu\text{m}$  operation is available by using a waveguide laser, ZnSe wire grid polarizer and analyzer, ZnSe modulator, and PbSnTe detector. A silicon Schottky barrier detector is also available to extend the range of the instrument in the ultraviolet to  $2400 \text{ \AA}$  and in the near infrared to  $1.1 \text{ }\mu\text{m}$ .

A theoretical analysis of the operation of modulated light ellipsometers was also undertaken. The results of the analysis were used to assist in determination of the specifications for the instrument to be built and allowed a substantial cost saving as a result of relaxation

of the usual angular position measurement requirement of ellipsometers. This saving was applied to the optics to allow the purchase of an instrument having a wider-than-normal wavelength range. In addition, an extensive computer program for the analysis of ellipsometer data was obtained from the Nation Bureau of Standards. It has been fully debugged and is now operational on the GE635 computer system although certain minor modifications have not yet been made to permit the handling of the data that will be generated by our modulated light instrument.

The basic operating principle of the instrument and a description of the 10.6  $\mu\text{m}$  components which were constructed was discussed in a paper presented at the Fourth Conference on High Power Infrared Laser Window Materials. The text of the paper is included in the appendix.

#### E. 10.6 $\mu\text{m}$ Laser Damage

The laser damage effort under the present ARPA-supported program started according to plan in the latter part of November 1973.

A review of our major accomplishments is best presented by reference to the preprints of two papers in the appendix of this report. The papers were given at the Symposium on Damage in Laser Materials, Boulder, Colorado, May 1974, and will be published in the proceedings of the Symposium. The material in this section covers much additional experimental detail and also includes results which were obtained after May 1974.

##### 1. Description of Laser Damage Testing Facility Laser

An ultraviolet preionized  $\text{CO}_2$  TEA laser developed at HRL provided the laser for this study.<sup>6</sup> It consists of a 50 cm x 50 cm x 2.5 cm discharge between a modified Bruce profile electrode and a flat electrode, as illustrated in Fig. 30. Preionization is accomplished by a row of resistively ballasted arcs on each side of the main discharge, controlled by a separate pulse forming network. Two types of pulsing networks were used, ignitron and thyatron switched,

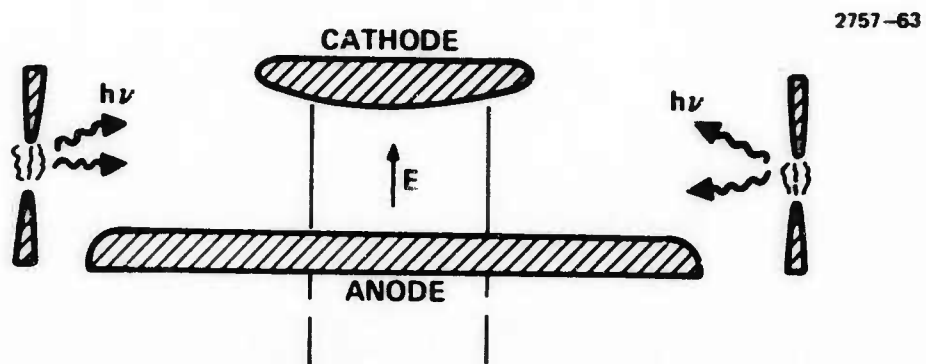


Fig. 30. Schematic of TEA laser cross section showing electrodes and preionizers.



as shown schematically in Figs. 31 and 32. The timing pulses for the preionizer and main discharges are generated in carefully shielded semiconductor timing circuits, with an adjustable delay, and amplified to a level sufficient to control the main switching tube.

The discharge cavity is contained within a vacuum-tight plexiglas cylinder 30 cm in diameter by 60 cm in length. Output Brewster windows with a 5 cm square aperture at each end permit external mounting of resonator optics. Gas impurities which initiate erratic output as a result of arcing are minimized by a  $25 \text{ m}^3/\text{hour}$  Balzer mechanical vacuum pump with oil trap which results in rapid evacuation of the system down to 10 m Torr. A gas handling system, illustrated in Fig. 33, allows a convenient choice between premixed gases or the low  $\text{CO}_2$  fraction mixes used for long pulse operation. Operation anywhere up to atmospheric pressure is possible with any mixture, with or without a continuous flow. Buildup of contaminants in the gas mix from electrical breakdown of  $\text{CO}_2$  during operation result in an eventual onset of arcing and erratic operation unless a continuous flow of new gas is provided or about 3%  $\text{H}_2$  is introduced into the mix.<sup>7</sup> Since operation with flowing conditions for months resulted in interruptions for replacement of gas bottles, later operations relied upon a sealed mix with 3%  $\text{H}_2$ , mixed by a fan within the laser chamber. This mix is discarded at the end of each day and has resulted in reliable operation.

The optical cavity consists of a 2.5 m approximately hemiconfocal cavity with a 5 m metal reflector and an uncoated Ge resonant reflector. An adjustable aperture set at about 1.2 cm selects the  $\text{TEM}_{00}$  mode while providing an essentially untruncated output. The discharge chamber, optical cavity, sample chamber, and optical train are mounted upon a ferromagnetic honeycomb table for maximum stability (Fig. 34). The uncoated Ge etalon provides a convenient output coupler of 78% reflectivity which does not suffer from the cumulative degradation with time experienced with commercial coatings. The development of this laser system for damage investigations has been supported by HRL and AFWL (F29601-72-C-0132) since 1972.<sup>8</sup>



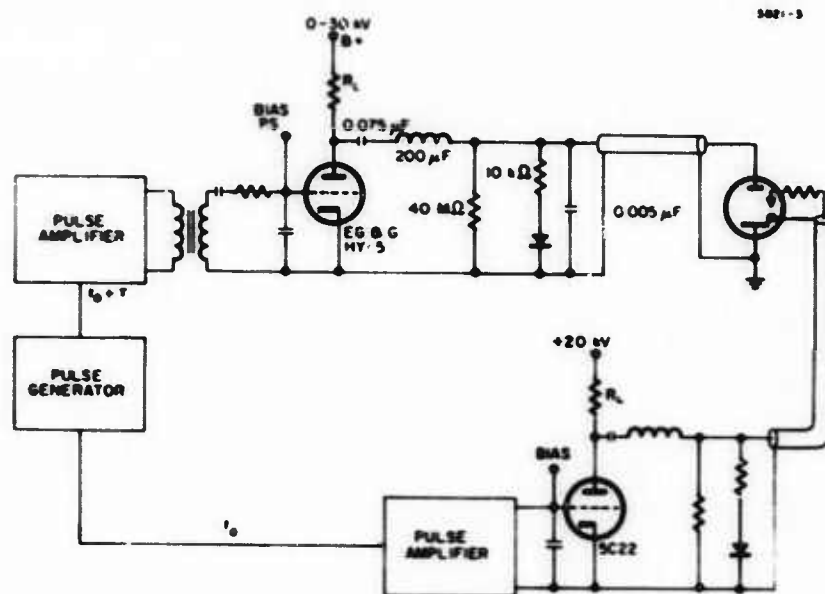


Fig. 31. Simplified schematic of double discharge electrical pulse forming network. Ignitron.

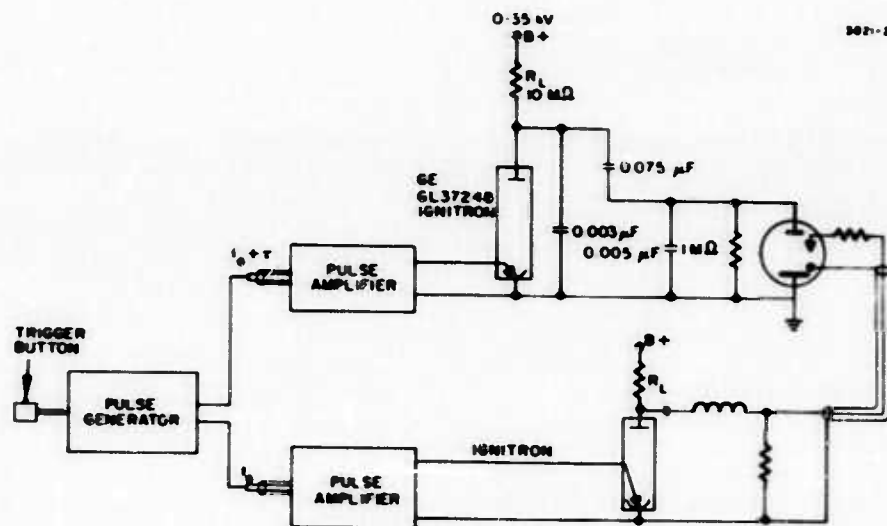


Fig. 32. Simplified schematic of double discharge electrical pulse forming network. Thyatron.

In summary, reliability for an extended period of time, shot-to-shot reproducibility, and the widest possible range of output energy and pulse length consistent with the above, were the criteria which governed the design of this device.

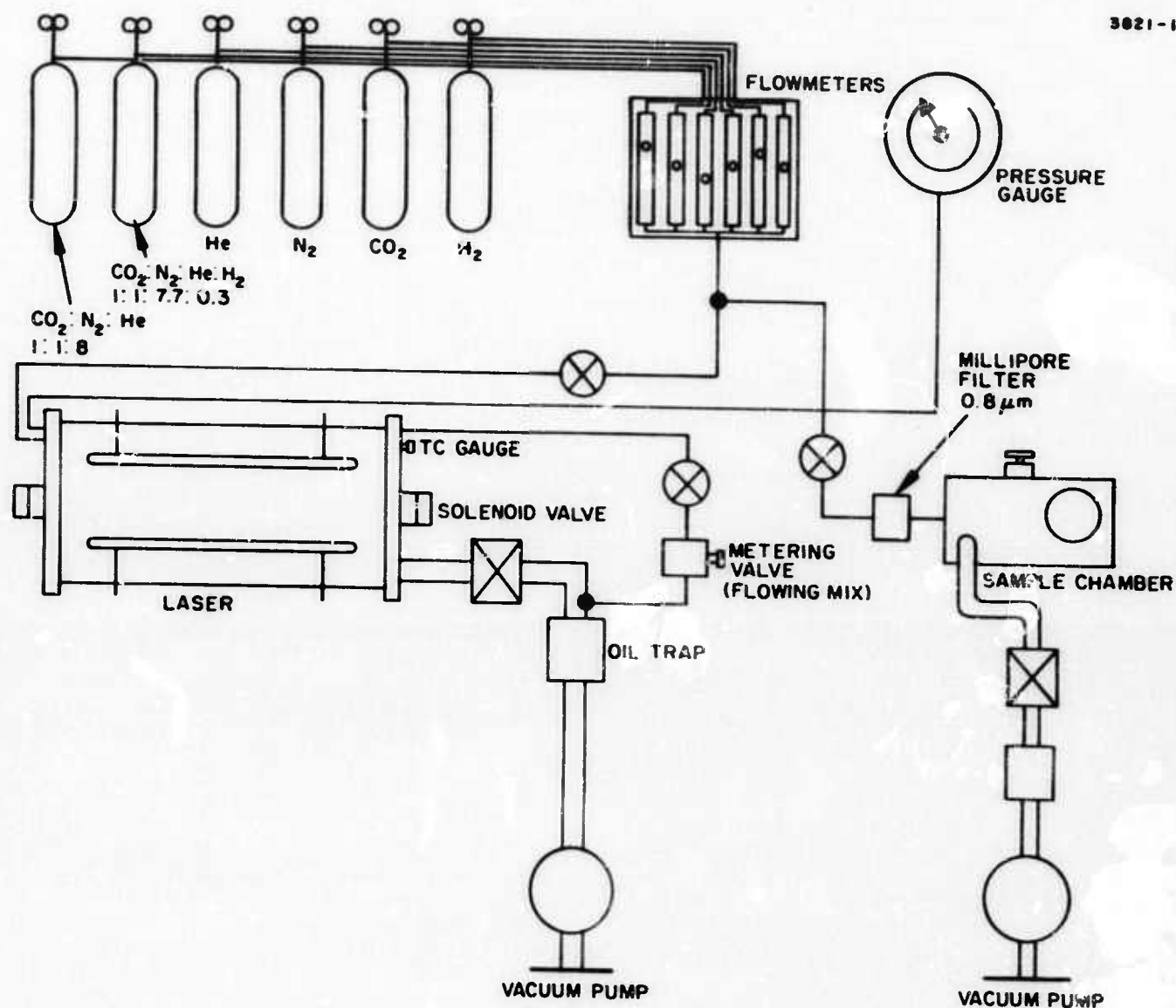


Fig. 33. Gas handling system.

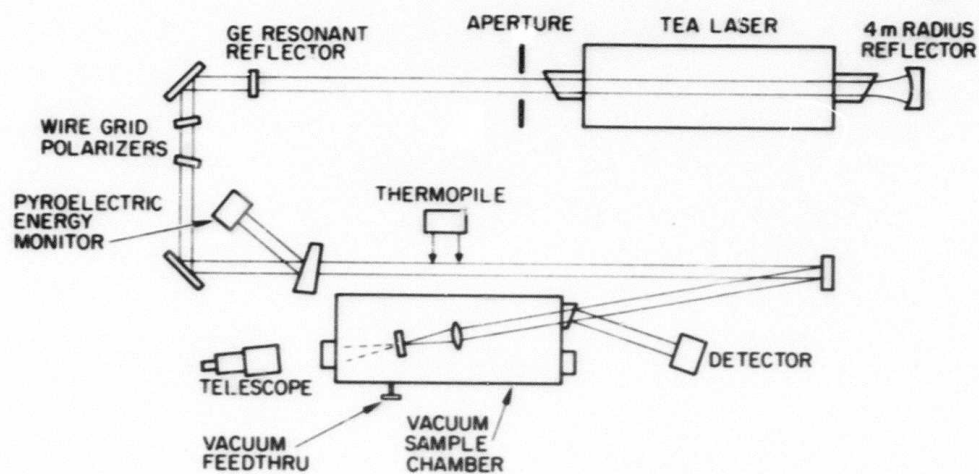


Fig. 34(a). Schematic of optical train.

M10713

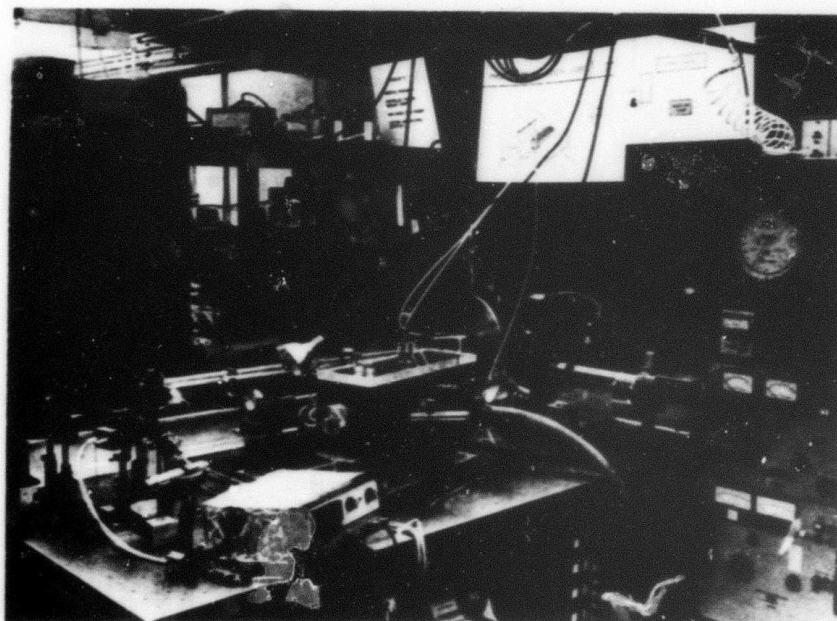


Fig. 34(b). Damage facility.

a. Polarizers — The damage resistance of the materials examined in this program vary over several orders of magnitude so crossed polarizers provide a desirable way of continuously varying the intensity. However, control of the discharge voltage has provided a satisfactory alternative within the limitations of laser operation and stability. Typically, control of input voltage allows a little over a 10 to 1 range of output energy, with a small change in temporal pulse shape toward the lower end of the discharge voltage range. There has been no evidence of change in spatial profile with pump voltage. Greater variations in energy density at the sample are accomplished by changes in focal length or usage of partially reflecting mirrors in the optical train.

Since birefringent materials for polarizers at  $10.6\ \mu\text{m}$  are difficult to obtain, wire grid polarizers and stacked plate polarizers are two of the remaining options. Hughes Research Laboratory and Caltech have developed a technique for making holographically-exposed sputter-etched wire grid polarizers and diffraction gratings suitable for high power usage.<sup>9</sup> Utilizing our ZnSe finishing and AR coating technology a pair of 2.5 cm square polarizers on ZnSe were fabricated using gold wires of  $1\ \mu\text{m}$  thickness with a  $1\ \mu\text{m}$  space between wires. A chromium layer between the gold and the AR coating provides sufficient adhesion so that the samples can be scrubbed for removing photoresist or for cleaning. These samples possessed individual extinction ratios over 200:1 and a combined transmission of about 80%. Two polarizers are used so that the output polarization does not rotate with change in attenuation. These polarizers suffered damage after roughly a thousand shots. The replacements which have been generated and presently have an extinction ratio of about 50 should prove adequate.

b. Detectors — Total pulse energy and temporal pulse profile are monitored using a variety of pyroelectric and photon drag detectors in conjunction with a 500 MHz bandwidth EMI shielded Tektronix 7904 oscilloscope and fast camera system. Pulse shape is best monitored using a fast Rolfin 4 mm x 4 mm Ge photon drag detector

with a risetime of better than 1 nsec when used with a 50  $\Omega$  input Tektronix 7A19 preamplifier. This detector is also calibrated in terms of megawatts per millivolt output. A low sensitivity that requires the entire laser output is the only disadvantage of this type of detector.

Alternately, a pyroelectric detector with differentiator has also been employed. To gain sensitivity a 100 MHz video amplifier system with differentiation has been satisfactory. With a well-shielded amplifier assembly and two-stage differentiation to improve electrical noise rejection, this system possesses sufficient sensitivity to utilize a 4% fraction of the beam.

A variety of energy monitors has been used to calibrate and monitor the laser output. The primary standard consists of a Hadron Model 100 thermopile which utilizes a double-cone principle. This is used to calibrate a pyroelectric energy monitor which intercepts 4% of the beam from a wedged NaCl beamsplitter. Several strontium barium niobate (SBN) detectors were tried for the application, but their long term tendency to depole made them unacceptable. A polyvinyl-fluoride (PVF) plastic film on a metal substrate has proved to be completely stable with time up to this point. This detector, supplied courtesy of O. M. Stafsudd, UCLA, is mounted in a well shielded enclosure to suppress EMI, and has a sensitivity of less than 0.5 mJ when used with an EMI shielded oscilloscope. A recently acquired Laser Precision Joulemeter using a TGS pyroelectric detector is being used as a secondary standard. This device has a 1 cm active area multiple bounce light trap type of detector and supplies a direct digital readout. At present, agreement with our calorimetric standard is quite good (~10%) at full laser output, but electrical noise pickup through the case appears to be limiting the accuracy of the device at lower pulse energy. It is expected that eventually this device will speed the acquisition of data by eliminating the need for a photographic record on each shot.



c. Sample Chamber — Since the emphasis of this program is upon the development of high quality surfaces, contamination of these surfaces might play an important role in their damage resistance. An evacuated test chamber provides a controlled environment where testing can be conducted with a minimum of interference from the additional effects of dust, humidity, or air breakdown. In our previous studies it was found that the presence of a surface in the focused beam greatly lowered the threshold for air breakdown. This breakdown could both obscure the true damage resistance of that surface, and affect the morphology of the damage. However, in long pulse applications, air breakdown may become a lesser problem. In addition, it was found that pure bottled and filtered nitrogen exhibited a much higher breakdown, at least in the absence of surfaces.

The sample chamber in these experiments consists of a black anodized box with three NaCl windows, and plastic portholes and top for illumination and viewing. A mechanical pump with oil trap evacuates the chamber to below 1 Torr, and bottled  $N_2$  is passed through a 0.8  $\mu m$  Millipore Corporation filter to refill the chamber, thus minimizing dust and other contaminants. Two vacuum feedthroughs provide access to an x-y-z translation stage for manipulation of the sample during testing. The laser beam enters through a wedged NaCl window and is focused by a Ge Laser Optics, Inc. (LOI) lens mounted upon a separate stage. The sample is typically retained on a V-block, and observed with a 6x telescope from a 1 m distance through the back port. The defocused beam is allowed to pass out the back port. This sample chamber can be seen in Fig. 34(b). An improved chamber, shown in Fig. 35 has also been prepared. This chamber includes additional flexibility and size so that better access, higher resolution microscopy, and better sealing can be achieved. Alignment tasks are eased by the incorporation of an optical rail within the chamber. Typically, samples are kept in clean containers to minimize the necessity for cleaning. Coatings and etched surfaces receive only a dusting from a 0.8  $\mu m$  filtered dry nitrogen jet.

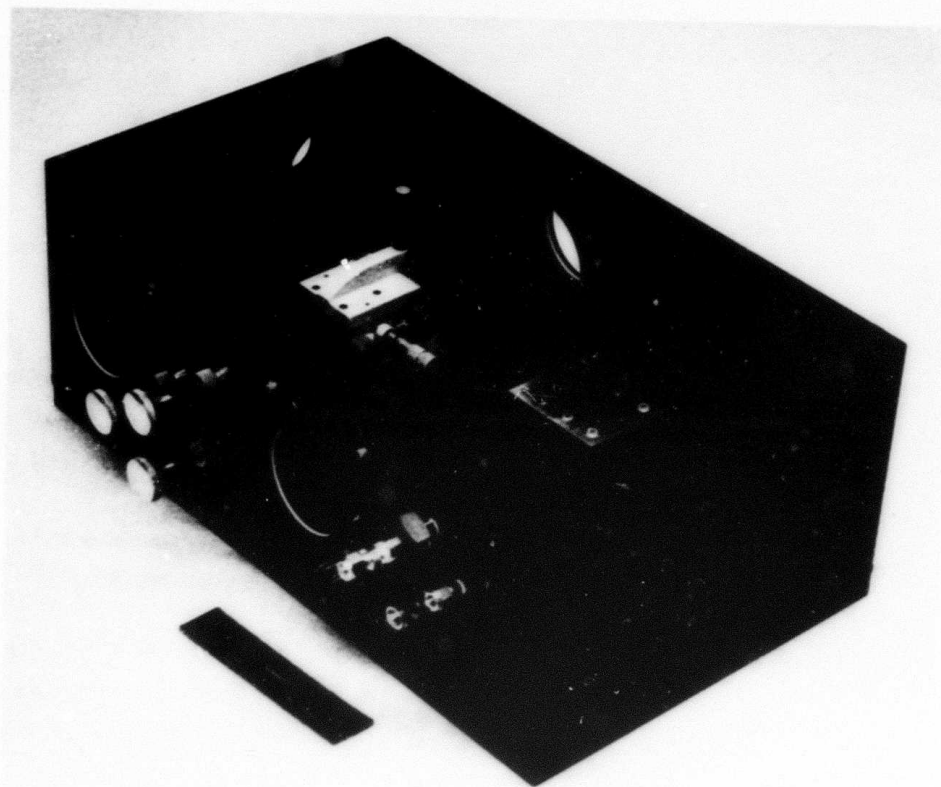


Fig. 35. Second model of sample chamber.



d. External Optics — Other optics within the optical train include a wedged NaCl beamsplitter for the pyroelectric energy monitors, partially transmitting coated Ge reflectors of 10 and 20% to make gross changes in laser energy, and a selection of LOI Ge focusing lenses from 1.5 in. f.l. to 10 in. f.l. The 5 in. f.l. lenses have been found to deliver diffraction-limited performance by actual spot size measurements, and the 2.5 in. f.l. lens has been very close to diffraction-limited. Measurements are pending upon the 1.5 in. f.l., but it is not expected to be diffraction limited. The techniques used to make these measurements are discussed in the paper presented in the appendix and previous reports.<sup>8,10</sup>

Visible in Fig. 34(a) is the He-Ne alignment laser and some of the apertures used to define the laser axis, as well as an autocollimator. The beam is introduced into the optical train by means of removable pentaprism which directs the beam either to the laser or to the focusing optics.

e. External Diagnostics — It has been found that damage is not always accompanied by a visible plasma, and that the appearance of a plasma does not always indicate functional damage to the coating or substrate. To provide more careful evaluation of the effect of laser irradiation than possible within the sample chamber, several high resolution optical microscopes of up to 2000x are used to examine the samples after testing, among them phase contrast and polarizing microscopes. In addition, SEM and x-ray microprobe devices have been available, although the type of damage mechanisms explored during this program have not made this type of sophistication necessary at this point.

## 2. Laser Performance

a. Status — Continued improvement of 10.6  $\mu\text{m}$  thin film coatings and optical surfaces has made greater flux densities increasingly desirable. This has been achieved mostly by tighter focusing of the beam. The laser output has been refined to give 250 mJ

output in the TEM<sub>00</sub> mode at 0.6  $\mu$ sec and 200 mJ, at 4  $\mu$ sec. The cavity presently uses a 5 m radiused superpolished reflector and Ge flat giving an output  $e^{-2}$  intensity diameter of 6 mm. The beam is propagated 3 m further through the optical train to give a 7.5 mm diameter beam upon the focusing lens.

Control of a large number of operating parameters of the laser has been necessary to achieve the present output, pulse length, and pulse shape. Table III illustrates many of the parameters that were varied in pursuit of better control of the laser output. Some relevant changes which improved those desirable aspects of the laser output include electrical pump pulse shape and duration, electrode profile and spacing, gas mixture and pressure (especially CO<sub>2</sub> fraction and the addition of H<sub>2</sub>), and a modest increase in mirror radius.

As an example of an unsuccessful combination, a method to increase pulse length utilizing a high reflectivity output coupler (R 90%) and a low CO<sub>2</sub> fraction,<sup>11</sup> did not yield adequate output for our experiments when used in conjunction with single transverse mode control.

b. Longitudinal Mode Control Experiments — The CO<sub>2</sub> TEA laser used in the damage test facility operates in several longitudinal modes. The result of this multilongitudinal mode operation is that the temporal output of the laser is modulated, i.e., it consists of a series of temporal spikes as shown in Fig. 36(a). It has been considered desirable from the standpoint of achieving carefully controlled experimental conditions to operate the laser in a single longitudinal mode which would result in a temporally smooth output pulse. This kind of operation would allow more meaningful assignment of power densities to damage threshold measurements than has been possible to date with multimode operation.

An effort has been expended on this program to achieve single longitudinal mode operation of the CO<sub>2</sub> TEA laser with only moderate success. We have attempted to carry out a number of modifications to the laser system in a systematic manner, but, because of the limitations of the damage study subtask, have by no means exhausted all the

**TABLE III**  
**Laser Operating Parameters**

Parameters	Operational Constraints					
	Energy Output	Laser Pulse Duration	Laser Pulse Temporal Profile	Glow-to-Arc Transition	Alignment Stability	Transverse Mode Size/Profile
<b>Electrical</b>						
Pump pulse shape		X	X			
Pump pulse duration		X	X	X		
Pump pulse energy	X					
Timing of pump pulse relative to preionizer pulse				X		
Electrode profile				X		
Electrode spacing				X		X
Discharge volume	X					X
Discharge uniformity				X		X
<b>Gas mixture</b>						
Relative composition (CO <sub>2</sub> , N <sub>2</sub> , He)		X	X			
Total pressure	X	X				
<b>Optical cavity</b>						
Mirror reflectivities (Cavity Q, output coupling fraction)	X	X				
Cavity length		X			X	X
Mirror curvatures	X				X	X

T1568

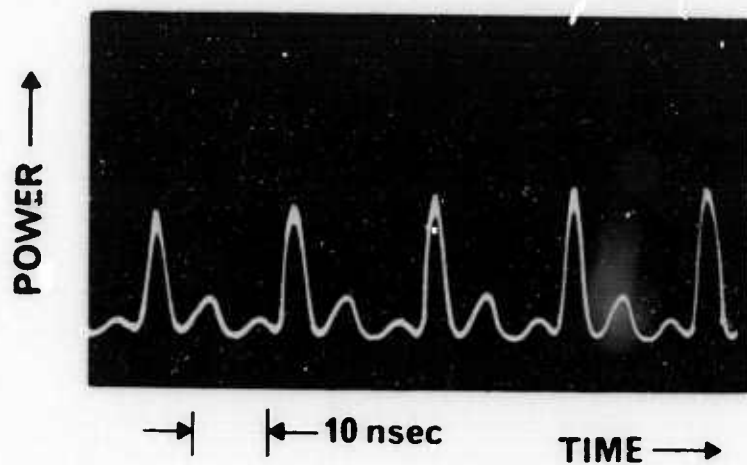


Fig. 36(a).  
Pulse shape mea-  
sured with photon  
drag detector.

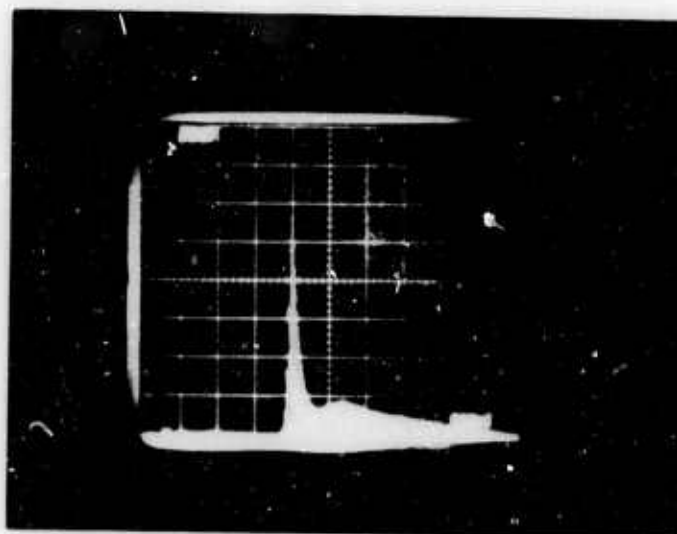


Fig. 36(b).  
0.6  $\mu$ sec equivalent  
pulse length.

experimental possibilities. As a result, the status at the present time is essentially the same as it was at the start of the program, i. e., the laser is well characterized with regard to the pulsed temporal output but does not operate in a single longitudinal mode.

Among the approaches taken toward the goal were the incorporation into the laser cavity of mode-selecting etalons, either in optical alignment with, or tilted with respect to, the cavity mirrors, a gas cell containing  $\text{SF}_6$  which has been reported to act as a saturable absorber at  $10.6 \mu\text{m}$  (saturable absorbers are known to act as longitudinal mode selectors when incorporated as intracavity elements), a number of variations of laser gas mix and pressure directed toward reducing the gain bandwidth of the active medium, and the incorporation of a low pressure  $\text{CO}_2$  discharge tube to act as an intracavity mode selector. A number of experiments were carried out in which the above approaches were employed alone or in various combinations with each other. Certain combinations of conditions yielded promising behavior regarding the temporal shape of the laser output but were usually accompanied by a degradation of another of the desired output properties of the laser. For example, the use of a combination of mode selecting intracavity etalons with a low pressure low gain gas mixture gave a desirable output pulse waveform suggestive of single longitudinal mode operation, but the total energy out of the system was too low to make it usable for most damage experiments of interest on this program. In addition to the previous example, it was found in a different series of experiments that the transverse mode of the TEA laser appeared to be distorted by the incorporation of the tube to be used as the low pressure discharge  $\text{CO}_2$  mode selector. None of the problems encountered is believed to be insurmountable, but within the constraints of this task it was not possible to pursue them to the extent necessary to achieve success.

It should be emphasized here that a single longitudinal mode laser is not essential to support a meaningful laser damage facility, especially if the multilongitudinal mode laser is well characterized

and monitored as is the case with the Hughes system. Nevertheless, single longitudinal mode operation is a highly desirable condition, and further attempts will be made to achieve this status on future damage activities at  $10.6\text{ }\mu\text{m}$ .

c. CO<sub>2</sub> Laser Pulse Duration Control — Until late in the program, the temporal envelope of the CO<sub>2</sub> laser output pulse used for damage studies has been the "typical" TEA laser pulse, i. e., a relatively short duration pulse consisting of a leading gain switched spike about 200 nsec wide followed by a longer tail (Fig. 36(b)). The equivalent pulse duration of these short pulses is about  $0.6\text{ }\mu\text{sec}$ . (The equivalent pulse duration is defined as the width of the square pulse whose height is equal to that of the gain switched spike and whose total energy is the same as that of the laser pulse. See Fig. 37.)

During the latter stages of this program a series of modifications was undertaken that was directed toward obtaining longer output pulses. The ability to utilize the pulses of different duration for damage measurements is important for assessing the kinds of mechanisms that might be operative in the damage process. The approach that was taken utilized a combination of varying the laser gas mixture and total pressure and modifying the electrical pumping scheme. At present it is possible to operate the laser with a long output pulse (FWHM of  $6\text{ }\mu\text{sec}$ , equivalent rectangular pulse of  $4\text{ }\mu\text{sec}$ ) having a total output energy comparable to that for short pulse operation. The equivalent pulse length allows direct comparison of peak power in these two pulses by simply dividing energy density by equivalent pulse length. The long pulse operating condition utilizes a gas mixture consisting of 30 Torr CO<sub>2</sub>, 90 Torr N<sub>2</sub>, 20 Torr H<sub>2</sub>, and 310 Torr He. In this mixture the height of the gain switched spike is lowered relative to the pulse tail by utilizing a lower percentage of CO<sub>2</sub> and the addition of H<sub>2</sub> minimizes the need for flowing the gas or frequent replacement of the mixture. In addition to changing the gas mixture, it was found that it was also necessary to modify the electrical pumping scheme in order to sustain the transverse discharge for a longer period of time.

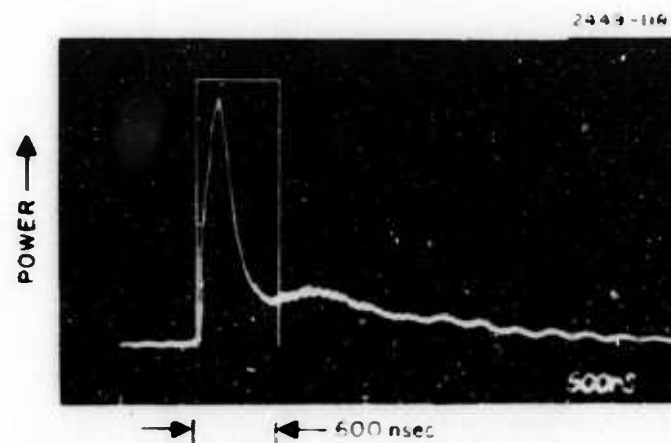


Fig. 37. Definition of equivalent pulse.



### 3. Damage Experiments

At the present stage of development considerable uncertainty exists in the nature of damage at  $10.6\text{ }\mu\text{m}$ . This section attempts an experimental exploration of some of the mechanisms for damage as well as obtaining numbers which characterize the performance of optics developed in the program. Bulk properties of three alkali halides have been examined at two wavelengths and two pulse lengths. The effects of surface finishing upon RAP-KCl has been studied (see appendix), and the damage threshold of a select number of films and AR coating designs have been measured (see appendix).

Details of these investigations are reported in these papers and the following sections represent a summary of this effort.

c. Alkali Halides — The alkali halides are the most nearly perfect materials available for transmission at  $10.6\text{ }\mu\text{m}$ . With their wide band gaps and very low intrinsic absorption, they are the only materials we have examined which might be expected to fail by some type of nonlinear electron "avalanche" mechanism. The measured breakdown fluxes of these materials in the bulk is typically well in excess of other film materials, most surfaces or air breakdown. Some previous work has been done at  $0.69\text{ }\mu\text{m}$ ,  $1.06\text{ }\mu\text{m}$ , and  $10.6\text{ }\mu\text{m}$  by Bass, Fradin, and Yablonovitch.<sup>12-14</sup> These measurements were performed upon commercially available materials, as were the 1937 dc measurements of von Hippel.<sup>15</sup> Recent advances in the processing of halides by reactive atmosphere processing (RAP) have allowed a considerable reduction in the number of foreign impurities in these crystals, and a consequent reduction in the  $10.6\text{ }\mu\text{m}$  absorption arising from these impurities.

By testing a representative sample of these materials in our  $0.69\text{ }\mu\text{m}$  and  $10.6\text{ }\mu\text{m}$  laser damage facilities we hoped not only to verify prior work, but to determine what, if any, effect might be gained by the improved material purity of RAP halides.

We have been able to determine that damage in these halides does not appear to be a simple parameter which can be directly related only to the material and its band gap. The data we have gathered do not fit the pattern of avalanche breakdown or an intrinsic process with an upper limit of breakdown for each material. While many questions about the materials used and the experimental conditions themselves still remain at this point, what can be concluded from the following results is that, as a practical matter, damage in a given halide is definitely material dependent.

b. Bulk Breakdown -- There has been a growing acceptance that laser induced breakdown in solids is the result of electric avalanche effects,<sup>16</sup> with hot electrons and band gap ionizing collisions providing the bootstrapping mechanism. It has been suggested by R. W. Hellwarth of USC<sup>17</sup> that optical breakdown at high field strengths is the result of impurity mediated electron multiplication. Material process control might thus have the effect of increasing the damage threshold beyond those values reported in the past.

Application of this model to NaCl seems encouraging.<sup>18</sup> In this model laser excitation of cold electrons tightly coupled to the crystal lattice by phonon interactions provides electron multiplication through relatively shallow electrons supplied by impurities. While it could not be said these experiments can differentiate between these two models, tests at two pulse lengths can distinguish between dielectric breakdown, or enhanced dielectric breakdown, and heating damage from inclusions. Pulse length dependence of avalanche breakdown has been predicted from the dc breakdown dependence of thickness by Yablonovitch and Bloembergen.<sup>19</sup> This model would predict that individual mode locked pulses of ~1 nsec might require ~8 times the power to cause damage, as the average envelope of a typical TEA laser pulse (~100 nsec). However, longer pulses (several  $\mu$ secs) would be expected to be practically pulse length independent. For our 10.6  $\mu$ m pulses, this model seems to predict that the average height of the

gain-switched leading edge pulse would control the breakdown, and thus a longer pulse would have the same power density damage threshold. An absorbing inclusion, on the other hand, would have dependence proportional to the square root of the pulse length due to the effect of heat diffusion away from the inclusion<sup>20-24</sup>. A simple linear absorption damage mechanism would have a breakdown proportional to energy density, independent of pulse length.

Tests were first performed at  $0.69\text{ }\mu\text{m}$  using a Q-switched ruby oscillator of TEM<sub>00</sub> transverse mode and single longitudinal mode, followed by an amplifier. This system, in operation for five years, is very well characterized and puts out a smooth pulse of 17 nsec.<sup>10</sup> The output intensity is controlled by a pair of glan prism attenuators and focused by a short focal length 3.8 cm lens to keep beam power below the self-focusing threshold. Under these focusing conditions the beam was sufficiently convergent that breakdown in the bulk of 6 mm thick crystals occurred before surface breakdown. Because of the small spot size of the focused beam, spot size measurements for this lens were difficult (diffraction limited spot size of  $7\text{ }\mu\text{m}$  at  $e^{-1}$  intensity points) and the initial results obtained are too tentative to be reported here with any confidence. Since further measurement of this important parameter is planned, the present results are presented in normalized relative units, rather than making the common assumption of a diffraction limited spot size which can result in large ( $\sim 10\times$ ) errors in power densities compared with measured spot sizes. Table IV summarizes measurements at  $0.69\text{ }\mu\text{m}$  and compares these with measurements at  $10.6\text{ }\mu\text{m}$ , made at two pulse lengths, and measurements made by other researchers. The last column includes early dc electric measurements made in 1937.

In several ways these new tests at  $0.69\text{ }\mu\text{m}$  and  $10.6\text{ }\mu\text{m}$  give unexpected results. The orderly progression of increasing damage threshold with increasing band gap suggested in the avalanche model advanced in Refs. 12, 13, and 14, does not appear quite so clearly in our data. The trend at  $0.69\text{ }\mu\text{m}$  does, however, agree with previous

TABLE IV

Relative 0.69  $\mu\text{m}$  and 10.6  $\mu\text{m}$  Electric Field Breakdown Thresholds for Three Commercial and High Purity Alkali Halides  
(Normalized to Kyropoulos NaCl)

Material	HRL (1974)			Refs. 12 and 14 (1972)		Ref. 15 (1937)
	0.69 $\mu\text{m}$ $\tau = 17 \text{ nsec}$	10.6 $\mu\text{m}$		0.69 $\mu\text{m}$ $\tau = 14 \text{ nsec}$	10.6 $\mu\text{m}$ $\tau \cong 0.2 \mu\text{sec}$	
		$\tau = 0.6 \mu\text{sec}$	$\tau = 4 \mu\text{sec}$			
KBr	0.82	0.25	0.15	0.8	0.48	0.46
RAP-KBr	0.88	0.33	0.15			—
KCl	0.94 <sup>(a)</sup>	* <sup>(a)</sup> * <sup>(b)</sup>	* <sup>(a)</sup> * <sup>(b)</sup>	0.7	0.71	0.67
RAP-KCl	0.88	0.65 to 0.95	0.36			—
NaCl	0.47 <sup>(a)</sup> 1.00 <sup>(b)</sup>	0.54 <sup>(a)</sup> 1.00 <sup>(b)</sup>	— >0.38 <sup>(b)</sup>	1.00	1.00	1.00
RAP-NaCl	1.29	1.00	—			—
(a) Stockbarger (b) Kyropoulos *These tests invariably resulted in failure by inclusions.						

T1569

published experimental results. At  $0.69\text{ }\mu\text{m}$  the damage threshold appears to have very little variation between KBr and NaCl. On the other hand, in our results, there appears to be two distinct types of material available from Harshaw, at least for NaCl. The low quality material, sold as a spectrometer flat, and grown in air by the Kyropoulos method has a damage threshold four times higher (in power) than a relatively high quality strain-free material which is sold as a laser window and grown in vacuum by the Stockbarger method. In addition, only in the case of RAP NaCl is there any improvement of damage threshold over commercially available material. In all these tests at  $0.69\text{ }\mu\text{m}$ , the damage consisted of a single site, usually taken to indicate that inclusion damage was not a factor. To be more careful, perhaps all that should be concluded is that the damage threshold is fairly homogeneous over the dimensions of the focused spot. Conceivably, damage can still be initiated at submicroscopic areas of localized weakness, but these points are sufficiently finely distributed that each focal volume sees many such points and damages at its point of maximum intensity.

On the other hand, with the same crystals used at  $0.69\text{ }\mu\text{m}$ , tests at  $10.6\text{ }\mu\text{m}$  in Harshaw KCl were plagued with inclusion damage. Different samples of both grades yielded the same result. Thus, only the RAP damage thresholds can be taken as limited by "bulk" processes for KCl. Several possibilities can be advanced for the apparent paradox of consistent inclusion damage at  $10.6\text{ }\mu\text{m}$  but consistent bulk damage at  $0.69\text{ }\mu\text{m}$ , in the same crystal, and even in very nearly overlapping regions of that crystal. The inclusions can be transparent at  $0.69\text{ }\mu\text{m}$  but absorbing at  $10.6\text{ }\mu\text{m}$ . The inclusions can be uniformly of a size roughly comparable to the thermal diffusion length of NaCl for the  $1\text{ }\mu\text{sec}$  pulse length of the  $10.6\text{ }\mu\text{m}$  laser, but too large to effectively couple with the relatively short  $\sim 20\text{ nsec}$  pulse of the  $0.69\text{ }\mu\text{m}$  laser. The inclusions could be spaced sufficiently distant that within the tests made here they were always missed by the small focal volume at  $0.69\text{ }\mu\text{m}$ , but with the far larger focal volume at  $10.6\text{ }\mu\text{m}$ , they were always hit (focal volume ratio =  $(\lambda_1/\lambda_2)^3 = 4 \times 10^3$ ).



It is not presently known how these inclusions were avoided in previous tests at  $10.6\text{ }\mu\text{m}$  by Yablonovitch.<sup>14</sup>

Potassium bromide exhibited a well behaved threshold which was a factor of 10 lower (in power) than NaCl for the  $0.6\text{ }\mu\text{sec}$  pulse. In short, the  $10.6\text{ }\mu\text{m}$  results differed remarkably from those at  $0.69\text{ }\mu\text{m}$ , despite the usage of the same crystal in many cases. As an incidental comment, it might be mentioned that the size of damage sites at  $10.6\text{ }\mu\text{m}$  was orders of magnitude larger than those at  $0.69\text{ }\mu\text{m}$ , probably as a result of the much longer pulse length and thus greater energy density.

The results at  $10.6\text{ }\mu\text{m}$  are presented in more detail in Table V. Tests were conducted at two pulse lengths upon both commercial and high purity materials. The 1.5 in. f.l. lens used in these tests is not diffraction limited, but has an rms wave front aberration of  $0.13\text{ }\lambda$  over its aperture. Since spot size measurements of this lens are still in progress the on-axis intensity of this lens has been tentatively estimated at 0.38 times the diffraction limited intensity by the Strehl intensity approximation<sup>25</sup> and the entries in Table V are based upon this number. In the case of NaCl available power density at the longer pulse length was insufficient to reach the breakdown threshold so these tests will have to await planned improvements.

While the results exhibit a general tendency for higher breakdown threshold with wider band gap, the present results seem inconclusive because of the wide variation of breakdown threshold with different commercial samples, and in the case of NaCl, with different sites on both Harshaw and HRL materials. If any conclusion can be drawn at present, it appears that the individual quality of the materials is not fully under control at present, and until this can be accomplished, reproducible damage thresholds will not be achievable.

As discussed previously, the damage mechanism would be expected to have differing pulse length dependences, depending upon the breakdown mechanism. For electric field dependent mechanisms being explored here, the power density breakdown would be expected

TABLE V

10.6  $\mu\text{m}$  Bulk Damage Thresholds for Three Alkali Halides at Two Pulse Lengths

Material	Damage Threshold (Power Density and Electric Field Strength)			Comments		
	Pulse length = 0.6 $\mu$ sec		Pulse length = 4 $\mu$ sec			
KBr	Harshaw	1.03 0.73	GW/cm <sup>2</sup> MV/cm	0.36 0.43	GW/cm <sup>2</sup> MV/cm	
	RAP-HRL	1.25/1.7 0.8/0.94	GW/cm <sup>2</sup> MV/cm	0.34/0.37 0.42/0.44	GW/cm <sup>2</sup> MV/cm	
KCl	Harshaw	<0.52 <sup>(a)</sup> <0.52 <sup>(a)</sup>	GW/cm <sup>2</sup> MV/cm	<0.046 <sup>(a)</sup> <0.15 <sup>(a)</sup>	GW/cm <sup>2</sup> MV/cm	Damage by inclusions
	RAP-HRL	— —		0.095 <sup>(b)</sup> 0.22 <sup>(b)</sup>	GW/cm <sup>2</sup> MV/cm	Damage by inclusions
NaCl	Harshaw	6.08 to 14 1.8 to 2.7	GW/cm <sup>2</sup> MV/cm	2.05 1.03	GW/cm <sup>2</sup> MV/cm	
	RAP-HRL	4.6 <sup>(a)</sup> 1.5 <sup>(a)</sup>	GW/cm <sup>2</sup> MV/cm	>2.3 <sup>(a)</sup> >1.08 <sup>(a)</sup>		
		12 to 16.0 <sup>(b)</sup> 2.5 to 2.9 <sup>(b)</sup>	GW/cm <sup>2</sup> MV/cm	— —		
		4.9 to 16 1.6 to 2.9	GW/cm <sup>2</sup> MV/cm	— —		
(a) Stockbarger (b) Kyropoulos						

T1570



to be independent of pulse length.<sup>19</sup> As can be seen for KBr this does not appear to be the case, thus further clouding the identification of damage mechanisms.

c. Surface Breakdown - The surfaces of good optical materials usually have a lower breakdown threshold than the bulk due to Fresnel reflections, enhanced flux densities on microcracks, pores, or polishing imperfections, or due to absorbing contaminants on the surface. Recent progress at HRL in raising the surface breakdown of KCl up to near the bulk breakdown has been described in a paper presented in the appendix of this report. It appears that polishing residue and the resultant surface damage are responsible for a surface threshold for failure over 30 times lower than the bulk threshold of the same material.

Etching of the surface with concentrated HCl by the method initially developed by J. W. Davison<sup>26</sup> has resulted in surfaces of greatly improved smoothness and lowered absorption (Fig. 38). The damage threshold of this type of surface was found to be much higher and generally more consistent. In addition, the morphology exhibited a marked change from one characterized by the appearance of a surface etching phenomena, Fig. 39, to one characteristic of bulk breakdown. In the latter case, Fig. 40, the damage site is relatively massive and fractured on a macroscopic scale. Table VI summarizes the results presented in the appendix. It was found that the etching had the additional desirable effect of decreasing the rate of fogging of the surface from atmospheric humidity, but that there is some increase in large scale waviness of the surface. It was also found that the care with which the surfaces were prepared affected the uniformity of results and that the quality of preparation improved with experience.

A similar high threshold was found for polycrystalline press-forged etched KCl, despite the existence of increased visible light scatter from the preferentially etched grain boundaries. This



Fig. 38(a). Etch polished HRL  
RAP KCl.



Fig. 38(b). Conventionally  
polished HRL RAP  
KCl.

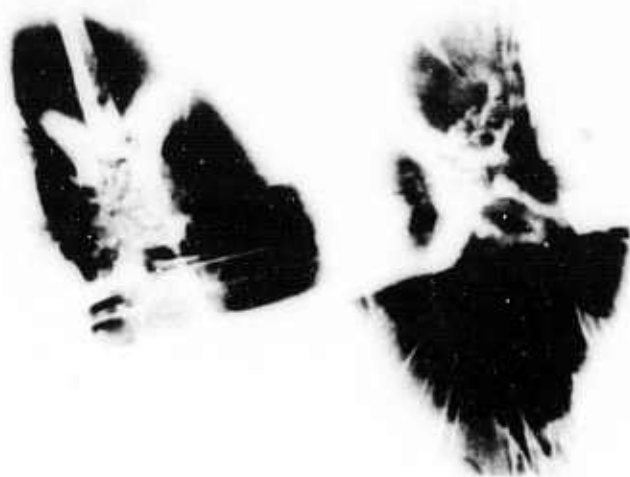


Fig. 39. Surface damage on conventionally polished KCl.



Fig. 40. Surface damage on etch-polished KCl.

TABLE VI

Surface Damage Thresholds for Polished and Etched KCl

Substrate and Surface	Bulk Absorption	Damage Threshold		Comments
		Energy Density, $\text{J}/\text{cm}^2$	Power Density, $\text{Gw}/\text{cm}^2$	
RAP KCl Polished Etched	0.0008 to 0.0020 $\text{cm}^{-1}$	70 to 350	0.12 to 0.58	Most sites over 1500 $\text{J}/\text{cm}^2$
	0.00013 to 0.00020 $\text{cm}^{-1}$	330 to 2700	0.55 to 4.5	
Press Forged KCl Polished Etched	0.00045 to 0.0021 $\text{cm}^{-1}$	—	—	Bulk damage by inclusions
	0.00022 to 0.00024 $\text{cm}^{-1}$	1500 to 1800	2.4 to 3.0	
Optovac KCl Polished Etched	0.001 to 0.002	18	0.03	Bulk damage by inclusions
	0.0004 to 0.00014	—	—	

T1571

scatter was not evident in  $10\text{ }\mu\text{m}$  scattering measurements performed on this program. Optovac KCl was found to be dominated by inclusions in the bulk, which very likely also contribute to the low surface damage threshold seen.

d. ThF<sub>4</sub> - The materials presently available which are suitable for use in a low loss AR coating at  $10.6\text{ }\mu\text{m}$ , are very limited and ThF<sub>4</sub> has proved to be one of the best candidates. Considerable effort has been expended to control process variables so that this material can now be reproducibly deposited in thin films which are free of foreign contaminants. With the rapid development of damage resistant high index materials of low absorption, the absorption coefficient of ThF<sub>4</sub> is the limiting factor in achieving lower loss coatings and, it appears, is also the limiting factor in the damage resistance of these AR designs. Depositions made under UHV conditions represent some of the most careful work that has been done to eliminate the effects of water vapor and other contaminants. For this reason, exploration of the damage mechanism and limitations of these films were carried out at two pulse lengths on KCl substrates.

Presented in Table VII are the results of some tests on UHV deposited ThF<sub>4</sub>. Deposition on KCl substrates not only permits a more accurate calorimetric determination of the absorption coefficient  $k$ , but etching of the KCl surface also permits testing of the film damage threshold without substrate damage or interference from polishing residue. The tests were performed using a 5 cm f. l. lens and laser output control by means of discharge voltage. Since previous measurements have always resulted in near diffraction-limited spot size measurements for this lens, the spot size used to generate the values in Table VII is based upon the calculated diffraction-limited spot size. Further calibration is planned since the wire grid polarizers are again available.

The test results presented in Table VII also represent the first tests performed at two pulse lengths at  $10.6\text{ }\mu\text{m}$ . While the measured absorption in these samples does not depart appreciably from

TABLE VII

Results of Laser Damage Resistance Testing of UHV Deposited ThF<sub>4</sub> on KCl

Sample	Deposition Material	Absorption	Laser Damage Threshold			
			0.6 $\mu$ sec Pulse Length			4 $\mu$ sec Pulse Length
			Energy Density, J/cm <sup>2</sup>	Power Density, MW/cm <sup>2</sup>	Energy Density, J/cm <sup>2</sup>	Power Density, MW/cm <sup>2</sup>
B70-3	Cerac ThF <sub>4</sub>	$k = 8 \times 10^{-4}$	300	500	300 to 400	75 to 100
B71-10	Cerac ThF <sub>4</sub>	$k = 1.08 \times 10^{-3}$	150	250	150	40
B71-12	Cerac ThF <sub>4</sub>	$k = 7 \times 10^{-4}$	300	500	280	70
B71-7	HRL ThF <sub>4</sub> (single crystal)	Not reduced	200 to 220	330 to 370	130 to 190	30 to 50
Single Crystal ThF <sub>4</sub>	—	$1 \text{ cm}^{-1}$	600	1000	500	800

T1572



conventional high vacuum deposited  $\text{ThF}_4$ , these damage thresholds appear considerably above the best previous numbers of  $80 \text{ J/cm}^2$ . A calculation of expected temperature rise based on the measured absorption indicates that these materials reach very close to their  $1100^\circ\text{C}$  melting point before damage is reached. They appear to be limited solely by their absorption, rather than any foreign inclusion, thermal stress, etc. A second confirmation of this postulate is provided by a comparison of the damage threshold at two pulse lengths. Since the energy density threshold is substantially the same for the two pulse lengths the mechanism appears to be independent of power density or pulse length, and dependent solely upon absorbed energy.

Included in Table VII is also a single crystal sample of  $\text{ThF}_4$  of material used to deposit B71-7. Its measured absorption of  $1 \text{ cm}^{-1}$  is quite high for a single crystal material, but presumably represents the intrinsic absorption  $10.6 \mu\text{m}$ . This sample was tested using the 1.5 in. f.l. lens, which presently has the uncertainties in spot size previously discussed.

The present result, reported here, lead to extremely high damage thresholds for a material of this absorption coefficient. Since a calculation of temperature rise in this material based upon its specific heat and absorption would indicate that the material should exceed its melting temperature, the present results must be viewed with reservation until a better estimate of spot size can be ascertained with this lens.

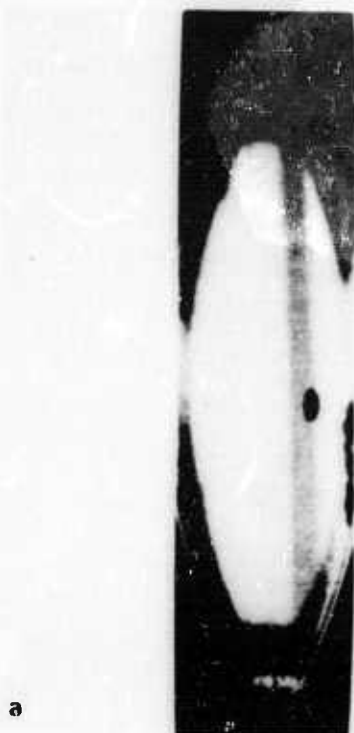
e. ZnSe - While this material has a good combination of mechanical and chemical properties, combined with moderately low absorption, its laser damage resistance has been limited by the presence of small absorbing voids or inclusions scattered throughout the material. In an attempt to determine the effects of improvement in this aspect of the materials preparation, an attempt was made to select regions of material freer of inclusions. An edge illuminated cross-sectional view of a typical sample reveals banding of the



inclusions as shown in Fig. 41. Earlier tests showed a dependence of damage threshold on apparent inclusion size and/or density. In addition, damage was often observed to occur at the entrance of the banded region of a sample, as shown. Therefore, an example of the best material now available was selected and sliced lengthwise into banded and unbanded regions. These were etch-polished, as is customary, and examined for inclusion density. Under a microscope, a particle density count revealed very small ( $\sim 50 \mu\text{m}$ ) particles in both banded and unbanded samples, with about a two-to-one ratio in particle density. Even the relatively clear "unbanded" slices still possess a large number of inclusions. For comparison, previous results reported in Ref. 8 are listed in Table VIII with these tests of select banded and unbanded samples. The unbanded sample, the last entry in the table, shows a modest 50% improvement over previous examples and the banded sample, but damage still occurs via localized inclusions. Other workers<sup>27</sup> have reached similar conclusions and have also apparently measured the "intrinsic" threshold by focusing between inclusions at  $1.06 \mu\text{m}$ . As will be seen, this low damage threshold is usually below that of the AR coating, and thus is the limiting factor at present.

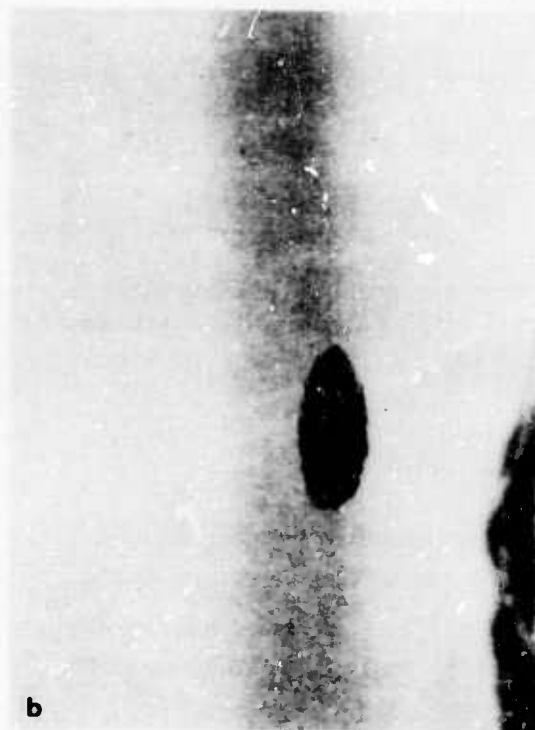
Zinc selenide film materials were also tested (see appendix), and on KCl substrates their damage threshold with small spot sizes ( $130 \mu\text{m}$ ) was found to be  $140 \text{ J/cm}^2$ . This test and tests of a variety of samples are tabulated in Table VIII.

f. As<sub>2</sub>S<sub>3</sub> - Previous exploration<sup>8</sup> had shown As<sub>2</sub>S<sub>3</sub> to be a good thin film material of high index. With one recent test in this program indicating a threshold of  $120 \text{ J/cm}^2$ , it has an absorption coefficient and damage threshold comparable with ZnSe. However, since it has no outstanding advantages and involves an additional difficulty in deposition due to sublimation at the high substrate temperatures desirable for ThF<sub>4</sub> depositions, no further tests of this material have been made at present.



a

2754-20



b

Fig. 41. ZnSe window damaged by a  $10.6\ \mu\text{m}$  pulsed laser beam. (a) Laser beam entry from right side of photograph (actual size). (b) Laser beam entry from right side of photograph (20x)

TABLE VIII  
Damage Thresholds in ZnSe

Sample	Absorption	Damage Threshold <sup>(a)</sup>		Comments
		Energy Density, J/cm <sup>2</sup>	Power Density, MW/cm <sup>2</sup>	
ZnSe R-417	0.02	5.6	9	Slightly opaque to eye. Very heavy inclusion density $\leq 125 \mu\text{m}$
ZnSe R-41	0.009	41	70	Dark inclusions $\leq 100 \mu\text{m}$ diameter
ZnSe R-7	0.0041	27	45	Light inclusions $\leq 50 \mu\text{m}$ , AR coated
ZnSe R-26	0.0030	30 to 40	50 to 70	"Banded" inclusion region
ZnSe R-26	0.0021	55	70	"Unbanded" region
Relative scattered 0% of above at $10.6 \mu\text{m}$ .				
(a) $\tau = 0.6 \mu\text{sec}$ .				

T1573

g. AR Coatings on ZnSe – As a final check upon the damage resistance that might be achievable in practical designs, two AR coating designs are discussed in the appendix. As expected, the limitation in both cases is set by inclusion damage from the substrate to 25 to 50 J/cm<sup>2</sup>.

### III. SUMMARY

The preliminary results we have achieved on our Laser Window Surface Finishing and Coating Technology Program have shown that consistently lowered 10.6  $\mu\text{m}$  optical absorption can be obtained for single crystal KCl and CVD ZnSe windows using the mechanical-chemical etch procedure we have developed. Improved laser damage resistance for KCl has been achieved and the damage to our present state-of-the-art antireflection coated ZnSe windows is bulk material limited and not limited by the window surface or coatings.

The results we have achieved for Ge film coatings indicate a pronounced dependence of the absorption coefficient on film deposition rate with Ge coatings on KCl held at 150°C showing evidence for K and Cl impurity migration into the films from the window substrate. The best Ge films we have produced are limited to an  $\alpha$  of  $\approx 10\text{ cm}^{-1}$ .

Correlations were found between the deposition rate, the impurity content, and physical structure of the films which appear to explain the 10.6  $\mu\text{m}$  absorption data. High deposition rates minimize the impurity content in the films and lead to amorphous film structure; both are required for low optical absorption at 10.6  $\mu\text{m}$ . A reduction of the KCl substrate temperatures from 150°C to 30°C markedly reduces the K and O levels in the germanium films on KCl.

Ion sputtering of  $\text{ThF}_4$  using pure argon ion beams results in films that are deficient in fluorine and have high optical absorption at 10.6  $\mu\text{m}$ . Reactive ion sputtering in argon-fluorine mixtures for  $\text{ThF}_4$  and other fluorides may be required to produce stoichiometric composition films.

Physical vapor deposition of  $\text{As}_2\text{S}_3$  on KCl was found to result in films of uncontrollable composition. Chemical vapor deposition was found to yield an amorphous  $\text{As}_2\text{S}_3$  layer along with crystallites of several As-S compounds.

Rutherford backscattering analysis has been shown to be a useful tool for investigating surface damage in single crystal KCl

caused by surface finishing operations and an equally useful tool for looking at impurity levels and stoichiometry in films. The unanticipated presence of the K and Cl in the Ge films produced on KCl focuses attention on the possibility that diffusion of species into film coatings from window surfaces and interpenetration of species in multilayer optical film coatings could have a pronounced effect on performance of coated infrared windows.

A modulated light ellipsometer was constructed for operation out to the 10.6  $\mu\text{m}$  wavelength region. It provides a unique capability for measurement of the optical constants of films and bulk materials.

Pulsed  $\text{CO}_2$  laser damage studies of (HRL) RAP grown KCl show an order of magnitude improvement in KCl surface damage for HCl-etched surfaces. In some KCl samples, KCl surface damage level approaches the bulk damage level. Surface damage levels  $>1500 \text{ J/cm}^2$  for 600 nsec pulses have been seen with bulk damage levels  $>3000 \text{ J/cm}^2$  at the same pulse duration. Previous damage data in the literature reported as intrinsic level, for KCl, probably were still impurity limited. Our damage, although higher in damage level, may still be impurity limited but appears closer to the intrinsic level.

Damage threshold in Raytheon CVD ZnSe have been shown to be limited by bulk imperfections.

## REFERENCES

1. N. Bloembergen and C. M. Stickley, Report of the ARPA 1972 Materials Research Council, E. E. Huckle, Editor, University of Michigan (1972).
2. M. Braunstein, A. I. Braunstein, and J. E. Rudisill, Proceedings, Conference on High Power Infrared Laser Window Materials, Carl A. Pitha, Editor (1972).
3. J. W. Davisson, Proceedings, Conference on High Power Infrared Laser Window Materials, Carl A. Pitha, Editor (1972).
4. M. Braunstein, J. E. Rudisill, and A. I. Braunstein, "Optical Coatings for High Energy ZnSe Laser Windows," Proceedings Third Conference on High Power Infrared Laser Window Materials, Carl A. Pitha, Editor (1973).
5. R. R. Hart, Radiation Effects **6**, 51 (1970); J. A. Davies, J. Denhartog, L. Eriksson, and J. W. Mayer, Can. J. Phys. **45**, 4053 (1967).
6. A. J. Palmer, W. M. Clark and J. Y. Wada, "Ultraviolet Preionized CO<sub>2</sub> Laser Research," Final Technical Report, AFWL Contract F29601-73-C-0107.
7. T. F. Deutsch, "Effect of Hydrogen on CO<sub>2</sub> TEA Lasers," Appl. Phys. Lett. **20**, 315-316 (1972).
8. "Low Absorption Coating Technology," Final Technical Report, AFWL Contract F29601-72-C-0132, Hughes Research Laboratories, December 1973.
9. H. L. Garvin and J. E. Kiefer, "Wire-Grid Polarizers for 10.6  $\mu$ m Radiation," presented at IEEE/OSA CLEA Conference May 30 - June 1, 1973, Washington, D. C.
10. C. R. Giuliano and D. Tseng, "Laser Induced Damage to Nonlinear Optical Materials," Final Report, Air Force Contract F33615-71-C-1715, September 1972.
11. A. Girard and A. J. Beaulieu, "A TEA CO<sub>2</sub> Laser with Output Pulse Length Adjustable from 50 nsec to Over 50  $\mu$ sec," IEEE J. Quantum Electron. June 1974.
12. D. W. Fradin and M. Bass, "Electron Avalanche Breakdown Induced by Ruby Laser Light," Appl. Phys. Lett. **22**, 5, 1 March 1973.



13. D. W. Fradin, E. Yablonovitch, and M. Bass, "Confirmation of an Electron Avalanche Causing Laser-Induced Bulk Damage at 1.06  $\mu\text{m}$ ," *Applied Optics*, 12, 4, April 1973.
14. E. Yablonovitch, "Optical Dielectric Strength of Alkali-Halide Crystals Obtained by Laser-Induced Breakdown," *Appl. Phys. Lett.* 19, 11, Dec. 1971.
15. A. von Hippel, "Electric Breakdown of Solid and Liquid Insulators," *J. Appl. Phys.* 8, December 1937.
16. N. Bloembergen, "Laser-Induced Electric Breakdown in Solids," *IEEE J. Quantum Electron.* QE-10, 3, March 1974.
17. R. W. Hellwarth, "Role of Photo-Electrons in Optical Damage," *Damage in Laser Materials* NBS Special Publication 341.
18. P. F. Braunlich and J. P. Carrico, "Feasibility Study of Exoelectron Imaging as an NDT Method for Laser Surface Damage of Nonlinear Optical Materials and Laser Glass," *Semiannual Technical Report No. 2, AFCRL Contract F19628-73-C-0032*, September 1973.
19. E. Yablonovitch and N. Bloembergen, "Avalanche Ionization and the Limiting Diameter of Filaments Induced by Light Pulses in Transparent Media," *Phys. Rev. Lett.* 29, 14, October 1972.
20. R. W. Hopper and D. R. Uhlmann, "Mechanism of Inclusion Damage in Laser Glass," *J. Appl. Phys.* 41, 10, September 1970.
21. Herbert S. Bennett, "Absorbing Centers in Laser Materials," *J. Appl. Phys.* 42, 2, February 1971.
22. M. Sparks and C. J. Duthler, "Theory of Infrared Absorption and Material Failure in Crystals Containing Inclusions," *1974 NBS Symposium on Laser Damage* (to be published).
23. David Milam, R. A. Bradbury, and Michael Bass, "The Role of Inclusions and Linear Absorption in Laser Damage to Dielectric Mirrors," *1974 NBS Symposium on Laser Damage* (to be published).
24. A. I. Braunstein, V. Wang, M. Braunstein, J. E. Rudisill, and J. Wada, "Pulsed Laser Damage Studies of Windows and Window Coatings," *NBS Special Publication 387, Laser Induced Damage in Optical Materials*, A. J. Glass and A. H. Guenther, Eds. (Government Printing Office, Washington, D. C., 1973).

25. Max Born and Emil Wolf, Principles of Optics (The MacMillan Company, New York, 1964).
26. J. W. Davisson, Conference on High Power IR Laser Windows, Vol. 2, 525-534, November 1972.
27. D. W. Fradin and D. P. Buz, "Laser-Induced Damage in ZnSe," Appl. Phys. Lett. 24, 11, 1 June 1974.

## APPENDIX

A list of papers presented and published during the period of work performance on the program are listed below.

1. M. Braunstein, "Laser Window Surface Finishing and Coating Technology," presented at the Third Conference on High Power Infrared Laser Window Materials, Hyannis, Massachusetts, 1973, published in the proceedings of that conference, Vol. III, AFCRL-TR- 74-0085(111) Special Reports, No. 174.
2. A.I. Braunstein, V. Wang, M. Braunstein, J.E. Rudisill, and J. Wada, "Pulsed CO<sub>2</sub> Laser Damage Studies of Windows and Window Coatings," presented at the Conference on Laser-Induced Damage in Optical Materials, Boulder, Colorado, 1973. Published in the proceedings, NBS Special Publication 387.
3. S.D. Allen, M. Braunstein, C.R. Giuliano, and V. Wang, "Pulsed CO<sub>2</sub> Laser Damage Studies of RAP Grown KCl," presented at the Conference on Laser Induced Damage in Optical Materials, Boulder, Colorado, 1974, published in the proceedings, NBS Special Publication 414.
4. V. Wang, J.E. Rudisill, C.R. Giuliano, M. Braunstein, and A.I. Braunstein, *ibid*.
5. S.D. Allen, A.I. Braunstein, M. Braunstein, J.C. Cheng, and L.A. Nafie, "Modulated Light Ellipsometer for Ultraviolet, Visible, and Infrared Measurements of Thin Films and surfaces," presented at the Fourth Conference on High Power Infrared Laser Window Materials, Tuscon, Arizona, 1974, to be published in the proceedings, abstract only.
6. M. Braunstein, A.I. Braunstein, D. Zuccaro, and R.R. Hart, "Ge and ThF<sub>4</sub> Films for High Energy Laser Components," *ibid*.
7. S.D. Allen, A.I. Braunstein, M. Braunstein, J.C. Cheng, and L.A. Nafie, "A 10.6  $\mu$ m Modulated Light Ellipsometer," presented at International Conference on Optical Properties of Highly Transparent Solids, Waterville Valley, New Hampshire, 1975, to be published in the proceedings by Plenum Press, edited by S.S. Mitra and E. Bendow.